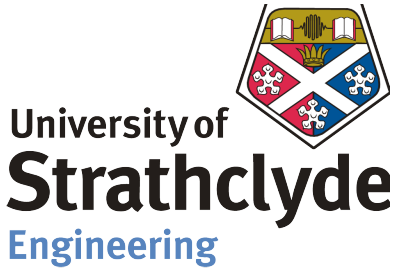

Department of Mechanical Engineering

Prediction of the Performance of a Contra-rotating Tidal Turbine

Author: David Charles

Supervisor: Dr Andrew Grant

A thesis submitted in partial fulfilment for the requirement of degree in

Master of Science in Energy Systems and the Environment

2009

COPYRIGHT DECLARATION

ACKNOWLEDGEMENTS

I am indebted a huge degree of gratitude to all those individuals who helped me throughout the duration of this thesis. A special thanks is due for Dr Andy Grant and soon to be Dr Tom McCombes for their unparalleled advice and expertise respect with the write-up and MATLAB aspects of this project. Without their help I would not have been able to obtain the results and arrive at the conclusions that I did. I would also like to thank my dad for his help and support towards the end, without which I would have been lost.

ABSTRACT

Sustainable energy generation through renewable sources is a rapidly expanding industry within the energy sector and as part of that industry tidal power creates the potential to tap into a previously untapped resource. Existing tidal barrage schemes are leading the way in exploiting tidal energy resources but are only producing a very small percentage of the world's generated electricity. Further development and expansion of this technology has been somewhat hindered by opposition from green political parties whom believe that the environmental impact of such a scheme is too great.

Tidal stream devices have therefore been developed as an alternative method of extracting the energy from the tides. This form of tidal power technology poses less threat to the environment and does not face the same limiting factors associated with tidal barrage schemes, therefore making it a more feasible method of electricity generation.

This thesis develops a Blade Element Momentum Model (BEMM) for a contra-rotating tidal turbine and discusses the merits and drawbacks of using such a device. It also investigates the potential of using different blade sections on the device and the resulting performance characteristics. The resulting BEMM code developed for this thesis is made user friendly through the use of dialog boxes and annotated figures. The end product of the code is easy to read performance plots commonly associated with turbine performance. Results from these plots for the Strathclyde contra-rotating tidal turbine (CoRMaT) suggest that NREL sections used in tidal turbine applications exhibit more desirable performance characteristics than NACA sections of a similar geometry.

TABLE OF CONTENTS

1 **INTRODUCTION.....1**

2 **TIDAL POWER.....4**

2.1 Gravity and the Tides.....4

2.2 Types of Tidal Capture Devices.....7

2.3 Fixing the Turbine in place.....7

2.4 Turbine Designs and Their Commercial Status.....8

2.4.1 Scotrenewables Tidal Turbine (SRTT).....9

2.4.2 Strathclyde's Contra-rotating Marine Turbine (CoRMaT).....10

2.4.3 Hammerfest Strøm's Blue Concept Tidal Turbine.....11

2.4.4 Lunar Energy's Rotech Tidal Turbine (RTT).....12

2.4.5 Open Hydro's Tidal Turbine.....13

2.4.6 Blue Energy's Vertical Axis Ocean Turbine.....14

2.5 Environmental Impact.....15

2.5.1 Water Quality.....15

2.5.2 Natural Life.....17

2.5.3 Significant Impact Factor (SIF).....18

3 **UNDERLYING THEORY.....19**

3.1 Fluid Mechanics.....19

3.1.1 Basic Equations.....19

3.1.2 The Boundary Layer.....19

3.2 The Betz Limit.....20

3.3 Blade Element Momentum Method.....22

3.3.1 Prandtl's Tip Loss Factor.....26

3.3.2 Glauert's Correction for High Values of a.....27

3.3.3 BEM Method Algorithm..... 29
3.3.4 Computing Thrust, Power and Root Bending Moment.....29

4 **CONTRA-ROTATING TURBINES..... 31**
4.1 A Brief History of Contra-rotating Turbines..... 31
4.2 Advantages of a Contra-rotating Turbine over Single Rotor Turbines.....32
4.3 ESRU's CoRMaT Design.....32
4.3.1 CoRMaT design Process.....33
4.3.2 Some Results from the CoRMaT Prototype Testing.....33

5 **HYDROFOIL SECTION SELECTION.....36**
5.1 Criteria for Tidal Stream Turbine Blade Design.....36
5.2 Material Selection and Geometric Considerations.....37
5.3 Hydrodynamic Performance Analysis of some commonly used Blade sections in Renewable Power Generation Devices.....38
5.3.1 An Introduction to NREL Section Families Used In Turbine Design.....38
5.3.2 Hydrodynamic Performance of NREL's S814 Section.....40
5.3.3 Hydrodynamic Performance of NREL's S815 Section.....43
5.3.4 An Introduction to NACA Section Families used in Turbine Design.....46
5.3.5 Hydrodynamic Performance of NACA's 63-1324 Section.....47
5.3.6 Hydrodynamic Performance of NACA's 63-1126 Section..... 50
5.4 Concluding Remarks on Blade Section Selection for a Tidal Stream Turbine..... 52

6 **MODELLING OF THE CORMAT & RESULTS..... 54**

6.1 Model Inputs and Parameters for a Single Rotor Device.....54

6.1.1 User-defined Inputs and Parameters..... 55

6.1.2 Blade Section Specific Inputs and parameters.....58

6.1.3 Method of Iteration Adopted.....59

6.1.4 Model Outputs..... 59

6.2 BEMM Model User's Guide.....61

6.3 Results and Discussion of Results for a Single Rotor BEMM Code.....62

6.3.1 Comparison of C_T – TSR Curves.....62

6.3.2 Comparison of C_P – TSR Curves.....63

6.4 BEMM Applied to a Contra-rotating Device.....65

6.4.1 Changes to BEMM Equations for First Rotor.....66

6.4.2 BEMM Equations for the Second Rotor.....66

7 **CONCLUSIONS AND FUTURE RECOMMENDATIONS.....68**

8 **REFERENCES AND BIBLIOGRAPHY..... 70**

TABLE OF FIGURES

Figure 1: Worldwide Tidal Constituent M2 taken from NASA on 6th June 2009..... 6
Figure 2: SRTT in "safe-mode" and in operation..... 9
Figure 3: ESRU's CoRMaT design on test rig.....10
Figure 4: Blue Concept Turbine.....11
Figure 5: Lunar Energy's RTT Design.....12
Figure 6: Open Hydro's Tidal Turbine Concept.....13
Figure 7: Blue Energy's Vertical Axis Ocean Turbine Design Concept..... 14
Figure 8: Control Volume containing streamtube around rotor..... 22
Figure 9: Blade Element Forces and Velocities.....24
Figure 10: Comparison of Momentum Theory Results with F=1..... 28
Figure 11: Combinations of NREL airfoil families sorted by generator size.....39
Figure 12: S814 Section shape created in JavaFoil..... 40
Figure 13: S814 Lift Curve Plotted over alpha range -5<alpha<179 at low and high Reynolds numbers..... 41
Figure 14: Figure 11: S814 drag polar plotted over alpha range -5<alpha<179 at a low and high Reynolds number.....43
Figure 15: S815 section shape created in JavaFoil.....44
Figure 16: S815 Lift Curve Plotted over alpha range -5<alpha<179 at low and high Reynolds numbers..... 45
Figure 17: S815 drag polar plotted over alpha range -5<alpha<179 at low and high Reynolds numbers..... 45
Figure 18: 63-1324 section shape created in JavaFoil.....48
Figure 19: 63-1324 lift curve plotted over alpha range -5<alpha<179 at low and high Reynolds numbers..... 48
Figure 20: 63-1324 drag polar plotted over alpha range -5<alpha<179 at low and high Reynolds numbers..... 50
Figure 21: 63-1126 section shape created in JavaFoil 50
Figure 22: 63-1126 lift curve plotted over alpha range -5<alpha<179 at low and high Reynolds numbers..... 51
Figure 23: 63-1126 drag polar plotted over alpha range -5<alpha<179 at low and high Reynolds numbers..... 52
Figure 24: CoRMaT Blade and Pitch distributions..... 57

Figure 25: Thrust Coefficient Performance Curves for NACA 63-1126 and NREL S814 Blade Sections for -2/0/2 Blade Pitch Angles..... 63
Figure 26:Power Coefficient Performance Curves for NACA 63-1126 and NREL S814 Blade Sections for -2/0/2 Blade Pitch Angles..... 64

NOMENCLATURE

a , a'	Axial inflow factor, tangential inflow factor
B	Number of blades
c	Blade chord
D	Drag
Δr	Radius of the Moon
F	Prandtl's correction factor
$\vec{F}$	Force vector
$\vec{F}_{ext}$, $\vec{F}_{press}$	C.V. External force, C.V. Pressure
$\vec{F}_{g}$, $\vec{F}_{t}$	Gravitational force, Tidal force
G	Universal constant of gravitation
K	Glauert's correction factor
L	Lift
m	Mass of the Moon
$\dot{m}$	Mass flow rate
M	Mass of the Earth and torque
P	Momentum vector and Power
r	Blade radial position
$\hat{r}$	Unit vector from the Earth to the Moon
R	Distance from the Earth's centre to the centre of the Moon
T	Thrust
$u_{1,} u_2$	Velocity at rotor, rotor wake velocity
U_{∞}	Freestream velocity
U_{θ}	Rotational wake velocity
$\vec{v}$, $\vec{V}$	Velocity vectors

Greek Symbols

α	Angle of Incidence
ω, Ω	local and rotor angular velocity
φ	Inflow angle
ρ	Fluid density
σ	Solidity
θ	Blade pitch angle

Coefficients

C_L , C_D	Lift coefficient, Drag Coefficients
C_P	Power coefficient
C_T	Thrust coefficient, non-dimensionalised projection of lift and drag forces into the normal and tangential direction

1. INTRODUCTION

The worldwide mentality towards energy generation methods has changed drastically in the last decade or so. This can be mainly attributed to an increased realisation of the contribution to recent climate change from fossil fuel generation and rapidly depleting supplies of oil, gas and coal. This change in mentality has sparked a shift from harnessing energy from fossil fuel sources to doing likewise from renewable energy sources such as wind, the oceans and the sun. A parallel increase in energy production through the alternative process of nuclear fission has also taken place in more affluent regions of the world.

This increase in carbon free energy production has been encouraged by national and international targets and incentives set by governments and international committees. These include the Kyoto Protocol and the EU commission whom have both laid out targets to be met by 2012 and 2020 respectively. These targets are mainly geared towards encouraging a worldwide reduction in green house gas (GHG) emissions.

The Kyoto Protocol to the United Nations Framework Convention on Climate Change was initiated in 1997 and came into effect on the 16th February 2005. Its objective is to achieve a worldwide reduction in GHG emissions by 2012, which is to be conducted primarily through the replacing of current carbon producing fuel sources with renewable energy sources. This is to be encouraged through setting national targets for emissions reductions and subsequent monitoring of GHG emissions.

The EU commission have developed a similar scheme in which EU member states are all required to meet national percentage reductions in emissions and percentage increases in renewable power production. These national targets combined are to make an average of 20% in both cases and are to be met by the year 2020. The EU commission have therefore come up with the apt slogan of "20 20 by 2020." The premise behind this scheme is that an increase in renewable energy consumption will lead to a decrease in GHG emissions. What sets this target aside from previously set EU targets is that it states that the reduction of emissions must be achieved by purely renewable sources and therefore nuclear energy and methods such as carbon capture and storage are not viable technologies for meeting the targets (EU commission (2008)).

It is these targets that have sparked increases in renewable generation across the globe, which has led to more sustainable energy supplies. However, with EU target dates growing ever nearer member states have opted to channel most funding into already commercialised renewable technologies such as wind. This is purely a short term solution and organisations such as Ofgem and National Grid have voiced their concerns about European countries becoming more reliant on wind technology (EU commission (2008)).

Wind energy is a perfectly acceptable short term solution to increases in energy demand and works well as a supplementary supply to country's main fuel sources but as a long term solution it is dubious whether it will work. The inherent intermittency of supply associated with wind power leaves the question to be answered: what happens when there's no wind? This is why it is important for member states that have alternative supplies of renewable energy available to them to utilise them as well.

The UK itself has some of the greatest tidal resources in the world and could potentially harness enough energy to supply approximately 10% of the country's current electricity consumption (Sustainable Development Commission (2007)). Tidal power does not suffer from the same intermittency problems as wind and is highly predictable, making it a steady supply of energy. The reason why UK energy companies are not utilising this resource to its full potential is because there are currently no commercially viable tidal stream energy harnessing devices.

It is therefore within marine energy companies best interest to commission a commercially viable tidal energy device. There are many prototype and drawing board designs out there but most that have reached testing stages are encountering problems. This is mainly due to problems encountered with the increase in fluid density between air and water. Technologies currently used on tidal stream devices are taken directly from wind turbines and problems with structural fatigue were encountered because of this density increase. Another important factor is the environmental impact of tidal energy devices and the constraints this may have on harnessing tidal energy. In comparison to wind power, tidal power could potentially have a much greater effect on the environment because of the greater degree of biodiversity surrounding tidal power schemes.

One technology that has not been tried and tested further than prototype stages but shows promising results in terms of a decrease in structural loads and a reduced wake structure is a contra-rotating

tidal turbine. One of the few of these in existence belongs to the University of Strathclyde and it has undergone comprehensive simulation and testing to ascertain the extent of these improvements in comparison to a conventional single rotor turbine.

This thesis aims to analyse the merits of a contra-rotating tidal turbine and investigate ways into which some of the inherent problems of tidal turbines may be overcome by using this alternative design. It also aims to investigate the importance of blade section choice and through the use of Mathwork's MATLAB produce a program to predict the performance of an arbitrary tidal turbine.

2. TIDAL POWER

2.1 Gravity and the Tides

The natural phenomenon known as the tides have been observed and noted for millennia and throughout history some of the worlds greatest minds have worked on solving the mystery of how the ocean is moved in such a way. Some of these minds belonged to the most influential men of their time and may be recognised from their theories and laws that govern the mathematics and physics world of today. These include Sir Issac Newton, Daniel Bernoulli, Leonhard Euler and Pierre-Simon Laplace to name but a few.

Newton was the first to offer a mathematical explanation of the tides in the *Philosophiae Naturalis Principia Mathematica* (1687). It was during his most well-known work on the theory of universal gravitation, which naturally lead to observations of the gravitational effects on the Earth from other planetary bodies. One of these said effects are the tides, which occur primarily because of the gravitational force experienced from both the Moon and the Sun by the Earth. Although the Earth does experience a gravitational pull from the other planets in our solar system (and technically every stellar and planetary body in the universe) these forces are negligible in comparison to those experienced from our own Moon and the Sun. In fact Venus has the most influence on the tides of the eight other planets. This gravitational force culminates in a mere $5x10^{-5}$m increase in the Earth's tidal range. To put into context how the Moon and Sun dominate the tides on Earth, Jupiter, the largest of the planets in our solar system, exhibits a tidal force ten times less than this (NASA (2000)).

The Moon and The Sun's effects on the tides themselves differ by approximately a factor of two. The gravitational pull of the Sun on the Earth is on average one hundred and seventy seven times that of the Moon, which would therefore lead you to believe that the Sun's effect on the tides would dominate the Moon's but the reality is quite to the contrary (A.C. Baker (1991)). The lunar tides dominate solar tides because of the disparity in distance and the fact that “the tidal force exerted by a body is proportional to the inverse *cube* of the distance to the source of gravity.” (NASA (2000)). Conversely gravitational force is inversely proportional to the *square* of the distance between the two bodies.

$$\vec{F}_g = -\hat{r}\, G \frac{Mm}{(R \pm \Delta r)^2} \tag{1.1}$$

$$\vec{F}_t = \hat{r}\, G \frac{2\, Mm \Delta r}{R^3} \tag{1.2}$$

Certain configurations of this Sun-Moon-Earth alignment are in fact the reasons behind spring (highest annually) and neap (lowest annually) tides. The first occurring when the Moon, Sun and Earth are in line (full and new Moon) and the latter occurring when the Sun and Moon are at right angles to each other, relative to the Earth (1st & 3rd quarters of the moon's cycle). Theoretically these tidal ranges occur in the ratio of 2.3:1 (spring:neap) but in actuality there are numerous factors that effect the tidal range at any one point on the surface of the Earth. These factors contributing to tidal variations are a result of the variety in orbital frequencies and are known as tidal constituents. Some of these constituents are:

- The Moon's elliptical orbit
- The Earth's elliptical orbit
- The Earth's axis of rotation being inclined to it's orbit around the Sun and likewise the Moon's orbit being inclined to the Earth's axis of rotation.
- Shallow water effects
- Atmospheric effects

The most dominant constituent in most locations on the Earth is the *principal lunar semidiurnal* constituent (a.k.a. M2), which most tide clocks follow. The map shown in Figure 1 shows the amplitude and phase of the tidal constituent M2 worldwide.

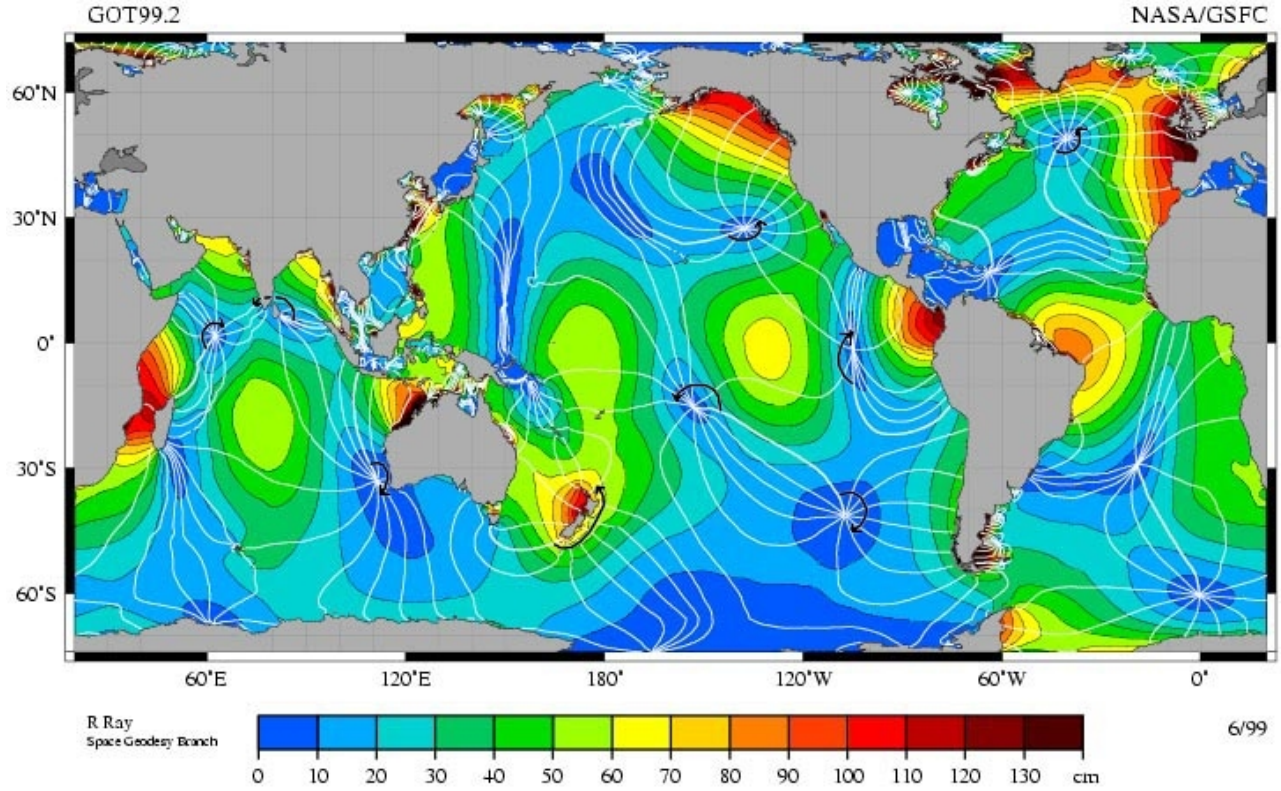

Figure 1*: Worldwide Tidal Constituent M2 taken from NASA on 6th June 2009*

The white lines in Figure 1 are known as *cotidal lines* and pass through points of constant tidal phase and therefore high tide is reached simultaneously at all points on a cotidal line. It can be seen that these lines eventually meet with other cotidal lines at a point, known as the amphidromic point, which is at once cotidal with high and low tides and is therefore satisfied with zero tidal motion. In addition to the tidal phase, the amplitude is also depicted by the use of the colour spectrum. The closer to the red end of the spectrum, the greater the amplitude of the tidal range at that point. It can be clearly seen that the Atlantic coast of western Europe boasts a consistently high tidal amplitude, which makes it a prime location for tidal power schemes.

The semidiurnal nature of the M2 tidal constituent makes it predictable to a certain degree and taking into account the other tidal constituents present at the location in question makes it possible to predict the annual change in phase and amplitude of the tides at that location. This therefore sets tidal power aside from akin methods of renewable energy conversion in that it can be predicted.

2.2 Types of Tidal Capture Devices

Most tidal turbines are based on rotating rotors, either of vertical or horizontal-axis configuration, that extract energy from the tidal stream by rotating around the x or z axis of a conventional x,y,z frame of reference system. These are often based upon the design of their closely related predecessors of the renewables industry, the wind turbine. In fact most tidal turbine hydrofoils are based on wind turbine's aerofoils because of the similarities in fluid properties of air and water.

A separate classification is often given to horizontal-axis turbines, which have flow enhancers such as diffusers or concentrators that act as streamtubes to maximise the amount of flow taken in by the rotor. Likewise oscillating hydrofoils are often categorised separately as these extract energy from the tidal stream by using hydrodynamic lift and oscillating in the z direction of a conventional frame of reference system. There are currently no commercially available devices but numerous designs are in the small-scale, prototype stage and a select few have been tested at full-scale level. A list of a few of the most promising designs from each of the three configurations currently under testing is described in section 2.4.

2.3 Fixing the Turbine in place

In order that a tidal turbine, extracting energy from the freestream flow, remains in roughly the same volume of water it must be moored to some stable, fixed structure i.e. the ocean floor or a floating platform. There are four conventional ways of achieving this and numerous unconventional methods (EMEC (2008)). The conventional methods are as follows:

1. **Seabed Mounted/Gravity Based**

   Physically attached to the seabed or if it consists of a large mass, this will anchor it to the seabed.

2. **Pile Mounted**

   Similar to the method used to mount large wind turbines. The vertical pile usually penetrates the ocean floor and the turbine can be raised out of the water when maintenance is required. The ability of horizontal-axis wind turbines to yaw is often transferred to the tidal turbines of the same orientation.

3. **Floating Mooring**

   This technique involves some sort of tethering to a fixed structure. These types of turbines can be categorised into three sub-categories:

   (i) *Flexible Mooring*: the device is tethered by a chain or cable to the seabed/mainland. This configuration allows the turbine to swing with the changing of the tide.

   (ii) *Rigid Mooring:* a fixed mooring system keeps the device in place, allowing little movement.

   (iii) *Floating Structure:* This method involves a central floating, anchored platform that can rise and fall with the sea level. Numerous turbines may be tethered to this structure by way of either (i) or (ii).

4. **Hydrofoil Inducing Downforce**

   This method utilises the downforce of numerous hydrofoils mounted on a frame to balance the overturning moment on the device and therefore keeping the device in place.

2.4 Turbine Designs and Their Commercial Status

Since Tidal power is an immature technology and no full-scale turbine installations are routinely providing power yet the commercial status is judged purely on the most promising technologies to date. Many different designs have been considered in recent years and some have been patented and tested at a prototype scale. One of the pioneering organisations of extraction of energy from tidal flows was the renewable energy consultancy by the name of IT Power. IT Power have been at the forefront of tidal power technology since the seventies and started out exploiting the river Nile's current flow to irrigate the farm land of Sudan. This demonstrated the potential of harnessing the kinetic energy of water currents and lead on to the idea of using this energy to generate electricity. The eighties then saw a quiet period for tidal power but the nineties saw an increase in interest worldwide. IT Power was leading research in Europe in the form of feasibility studies for tidal turbines and in 1998 the European Commission saw the potential in tidal turbine technology and started off the “Seaflow” project with a grant. Although IT Power had carried out a lot of the preliminary research for this project it required many investors to get off the ground, which resulted in a consortium of seven organisations funding the project (IT Power (2005)). Within this consortium were Marine Current Turbines (MCT), whom became sole owners of the intellectual

property rights for the Seaflow technology and developed the consequent commercial technology. Once developed to a satisfactory performance level in operation the 300kW Seaflow technology was installed 3 km off the North Devon coast. This momentous occasion occurred in 2003 and was a step in the right direction for tidal stream technology. Since then MCT have been working on a new 1.2 MW turbine technology called "Seagen" that has subsequently replaced Seaflow as the most powerful grid connected tidal current system, while also being the first marine energy project to secure ROCs accreditation. These two technologies have lead the way in tidal power and opened up the market to other competitors, challenging them to come up with their own novel and innovative designs. Some of these competitors in tidal current technology are listed below with their respective technologies.

2.4.1 Scotrenewables Tidal Turbine (SRTT)

One of these designs is Scotrenewables 1.2 MW floating tidal turbine, which consists of a single 32m long buoyancy tube with two horizontal axis turbines suspended beneath the structure. Each turbine has a 12m diameter rotor, the centre of which is 11m from the main structure.

This concept is designed for deep water operation of 25m or more and spring tide velocities of 2.5m/s to over 5m/s. This makes it a feasible technology for approximately 70% of the UK's tidal resource (Scotrenewables (2007)).

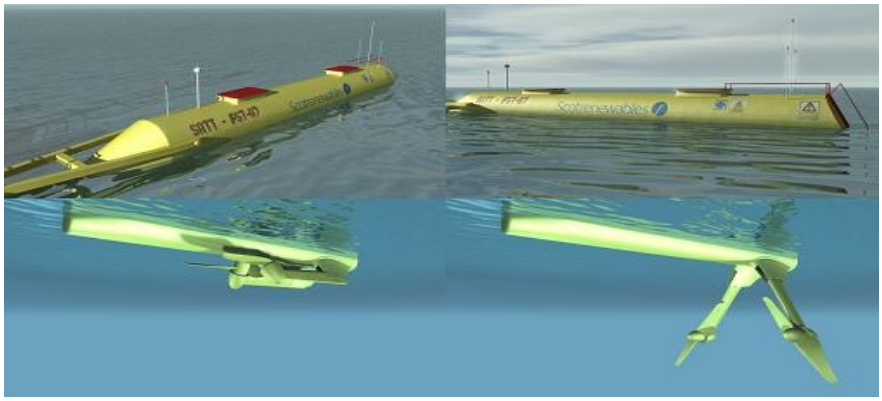

Figure 2: *SRTT in "safe-mode" and in operation*

2.4.2 Strathclyde's Contra-rotating Marine Turbine (CoRMaT)

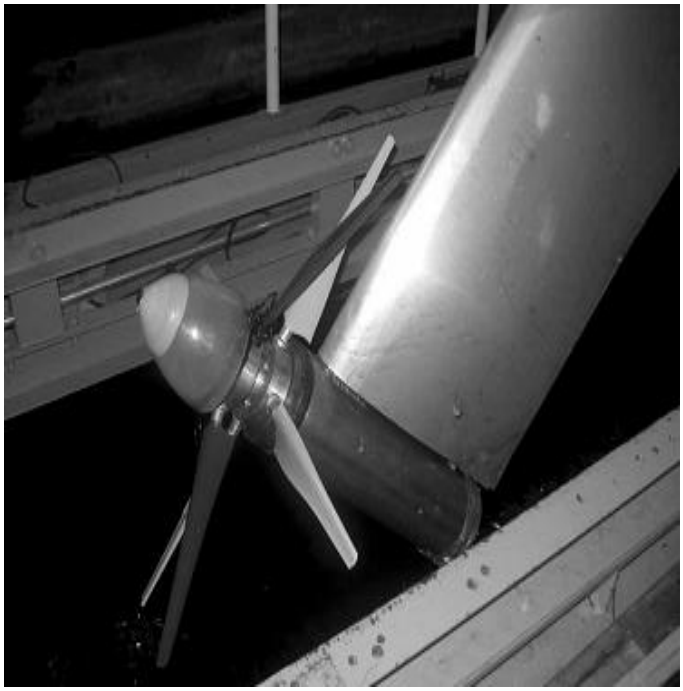

Figure 3*: ESRU's CoRMaT design on test rig*

Another promising horizontal-axis turbine design can be found within the Energy Systems Research Unit (ESRU) at the University of Strathclyde. This novel design incorporates two co-axial rotors that rotate in opposite directions. This therefore results in near-zero reaction torque on the supporting structure and mooring with the desirable side-effect of a decrease in turbulent wake, therefore potentially reducing the environmental impact as well as increasing the power output of the device. To date it has been through prototype testing at $1/30^{th}$ and $1/10^{th}$ scale with promising results.

2.4.3 Hammerfest Strøm's Blue Concept Tidal Turbine

Installed off the North Coast of Norway in 2003 Hammerfest Strøm's Blue Concept technology was in close contention with Seaflow to be the first commercial tidal technology in the water. It's function was mainly to gather data and it served this purpose until 2007 when it was temporarily decommissioned. However it is scheduled to be re-installed for further research this year (2009). It consists of a 300kW, variable pitch turbine designed to work in both flow directions of the tide and utilises a gravity foundation in order to minimise environmental impact and make for easy installation.

Figure 4*: Blue Concept Turbine*

2.4.4 Lunar Energy's Rotech Tidal Turbine (RTT)

Lunar Energy's RTT utilises a venturi duct to accelerate flow into the bi-directional horizontal axis turbine housed within the duct. This design (as shown in Figure 5) allows energy to be extracted from the tidal currents on both the ebb and the flood tides. Furthermore, the venturi duct channels water into the blades therefore increasing the volume of water that energy can be extracted from and eradicating the need for yaw and pitch control. The gravity base used to anchor the device to the seabed is taken from designs used in the offshore oil and gas industry and puts it's optimum operating depth at over forty metres. The simplistic design is aimed at keeping O&M costs down and allowing for quick, efficient maintenance checks.

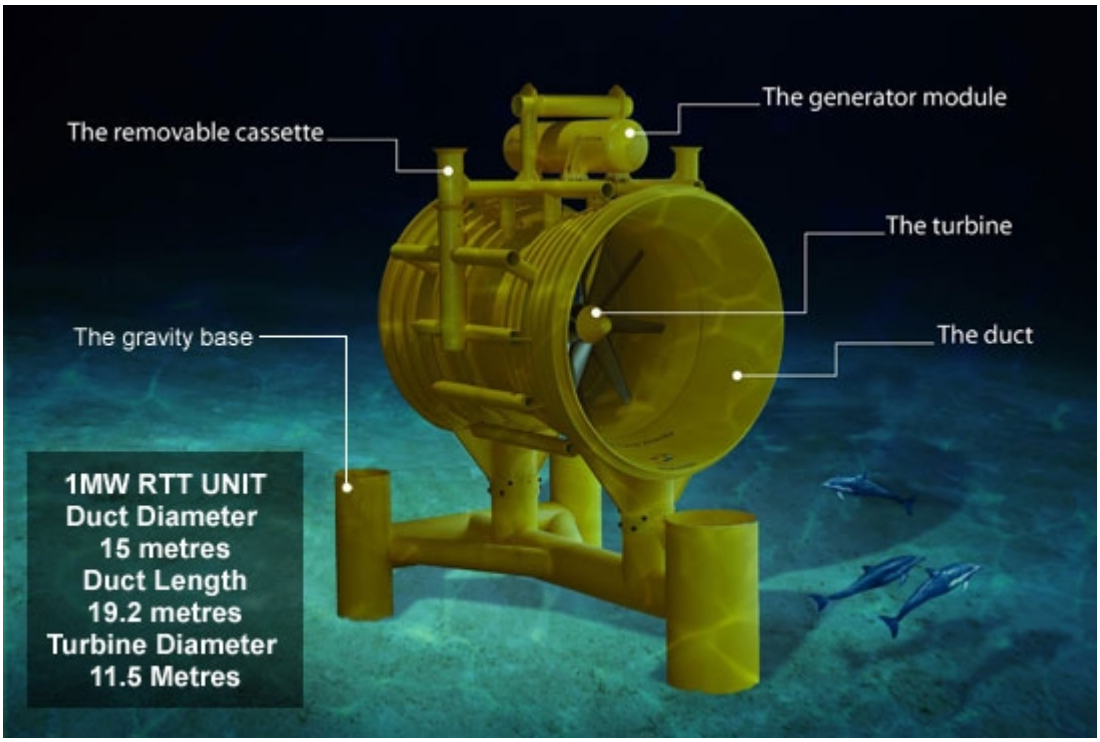

Figure 5*: Lunar Energy's RTT Design*

2.4.5 Open Hydro's Tidal Turbine

This other example of housing the turbine rotor within a duct follows a different design philosophy from that of Lunar Energy's RTT. Many aspects of this unique design are geared towards minimising the damage to the ecosystem within which they are installed and the marine life that inhabits that ecosystem. These design features include utilising an outer housing, which eradicates any potential danger from sharp blade tips; an open centre, reducing the radius of the blades and therefore providing an escape route for marine life and finally no use of lubricating fluids that could pose as a risk to marine life. Furthermore, alike the RTT, the Open hydro design is seabed mounted and therefore is not visually polluting in any way.

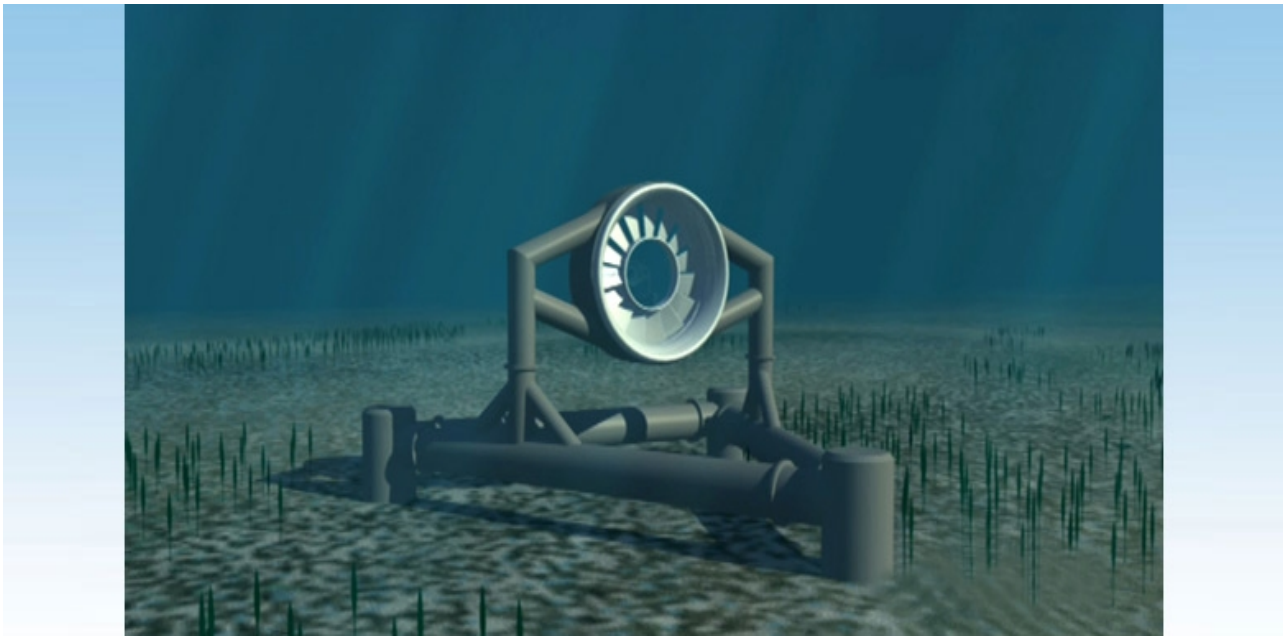

Figure 6: *Open Hydro's Tidal Turbine Concept*

2.4.6 Blue Energy's Vertical Axis Ocean Turbine

This vertical axis tidal turbine design acts differently, in comparison to the previous three designs, in the presence of tidal currents. Although the two designs both rely on hydrodynamic lift to turn, this design (see Figure 5) works such that it rotates in the same sense for both ebb and flow of the tide. The construction used in this design employs existing hydroelectric installation designs therefore reducing cost and improving reliability:

> *"The design of the Blue Energy Ocean Turbine requires no new construction methodology, it is structurally and mechanically straightforward."* (Blue Energy Canada Inc. (2008))

Proposed design architectures for this technology range from a single 5kW Micro Power System to an amply named Mega Power System that consists of a tidal fence capable of providing thousands of megawatts of power. The diversity of this technology implies it could be used in numerous power generation scenarios.

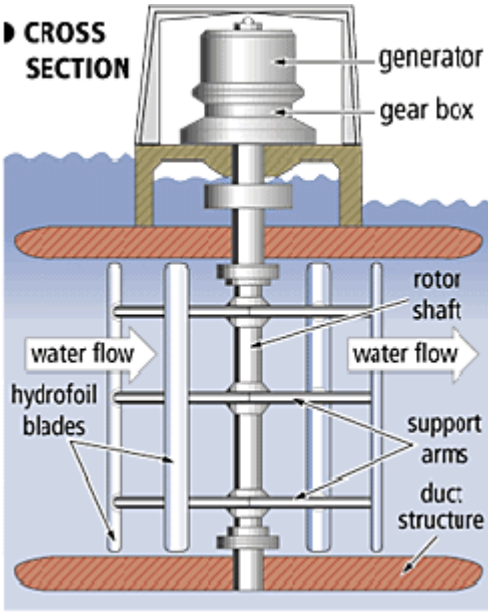

Figure 7: *Blue Energy's Vertical Axis Ocean Turbine Design Concept*

2.5 Environmental Impact

The environmental impact of a tidal power scheme is still not entirely known and in particular long term effects are merely speculation at this stage. However, it is logical to assume that a tidal power scheme may effect the environment in terms of water quality, which in turn would effect the marine life in close proximity. This is mainly applicable to tidal barrages, which are also proven to effect water levels and tidal ranges in the estuary or basin they occupy (Baker, A.C. (1991)). These impacts on the environment are not necessarily directly transferable to tidal stream devices such as the ones described in the previous section but let it be assumed, noting that the environmental impact of tidal power as a whole is largely speculative at this time, that to a certain degree they are.

The main consequences felt by the environment from tidal power devices stem from two fundamental characteristics of tidal turbines. These are that energy is extracted from the tidal flow and that turbulent wake is formed following the flow having reached the turbine. The implications of these factors are described in the following sub-sections.

2.5.1 Water Quality

There are numerous factors that may effect the water quality of a body of water used to supply a tidal power scheme. These can be categorised into 5 individual aspects, namely: Salinity, turbidity, pollutants, dissolved oxygen and bacteria.

Ocean salinity levels vary with global location from values of 30 grams/litre to values of 35 grams/litre. This, along with other variables such as water temperature, has a significant impact on the marine life within an ocean ecosystem and dictates what type of sea-life you will find in a specific location. It has been noticed from tidal barrages currently in existence, such as the one in the Severn estuary, that salinity varies from approximately 10grams/litre to 30 grams/litre. This is primarily due to fresh water inflows from rivers, or in certain locations heavy rainfall (such as you might expect during monsoon season), and has an effect on the marine life able to live in estuaries.

The suspected implications of installing a tidal power scheme in such an area are that the boundaries between fresh water and sea water move seaward. There is subsequently quite a small change in

salinity levels at any one point in the estuary, therefore making it easy for marine life to adjust (Baker, A.C. (1991)).

Turbidity is a term assigned to the measuring of the amount of particles suspended in a body of water and is a result of turbulence, convection and variation in water density. These particles may be of organic or inorganic composition but variations in turbidity of estuaries can be largely attributed to increases of sediment from river deposits. It is a fair assumption to make that the energy extracted from the tide by a tidal power scheme will result in a reduction in turbulent flow incurred by high water velocities. This would subsequently lead to a reduction in turbidity and therefore leaving clearer water. This would then allow sunlight to penetrate deeper into the water and greater growth of algae and plankton. It could therefore be said that, from a turbidity perspective, tidal power schemes will be beneficial to the environment.

However, a decrease in turbidity of a body of water will reduce the tidal excursion, that is to say the distance travelled by a single particle during a flood or ebb tide. This means that any pollutants in the area of water housing a tidal power scheme will take longer to leave that area and subsequently cause an increase in the amount of pollutants in circulation. These pollutants are often added to the water by industries located by the shore and may take the form of sewage or metals found in heavy industry. However, this increase in pollutants may be offset by the decrease in pollutants created by power generated through fossil fuels and nuclear power that may occur as tidal generating device take their place.

The concerns raised by increases in sewage levels may be partially alleviated by the mention of increased levels of light penetration in areas of water containing tidal power schemes. This increase in light penetrating estuary waters would aid in the destruction of bacteria, therefore reducing the risk of sewage related pollutants.

One of the main concerns with respect to water quality and it's effects on marine life is the amount of oxygen dissolved in tidal estuaries. It is crucial that this does not change drastically or it would have a profound effect on surrounding marine life. Simulations carried out on the proposed Severn estuary tidal barrage have been observed to have negligible effects on amounts of dissolved oxygen and therefore it was predicted that it would not have a profound effect on marine life (Baker, A.C. (1991)).

2.5.2 Natural Life

Given that most tidal power schemes are located near the shore it is safe to assume that the environmental effects will be primarily concerned with shallow water ecosystems. However, tidal power devices exist that are designed for deep water operation but it is assumed that the environmental impact of these technologies is significantly less. With this said, the three forms of life that would be expected to be effected most by the aforementioned change in water quality would be sea-life, birds and humans.

The risk posed by a tidal power scheme to sea-life is primarily dependant on the type of device installed. The different designs currently used have been developed with the aim of avoiding potential risks to sea-life and some of these designs can be seen in section 2.4. The reduction in turbidity resulting from the installation of a tidal power scheme could be beneficial in that it would provide more desirable breeding conditions for fish species such as plaice and flounders (Baker, A.C. (1991)).

Perhaps one of the greatest environmental impacts that a tidal power installation, such as a barrage, has on wildlife is the impact it has on wading birds. Wading bird's natural hunting ground, as you might guess from their name, is in the foreshore of estuaries where they feed on intertidal invertebrates in the mud. The effect of a tidal power scheme on these hunting grounds are summarised through looking at the proposed Severn Estuary tidal barrage. With the specific case of an estuary the effects will be primarily due to tidal barrages such as the one in the Severn estuary and not tidal stream devices. With this in mind it will be the change in tidal range that will be the main concern. Because wading birds hunt for prey in the foreshore any change to the area submerged would significantly change the amount of prey available in one tidal cycle.

At the top of the food chain are human beings and although changes in the ecosystem of the estuary are unlikely to effect surrounding human populations to any degree, the noise and visual pollution associated with a tidal power scheme may face objections. The short term nuisance would be the construction of the device(s), although this would most likely only effect residents right on the coast and therefore unlikely face any objection. However in the long term tidal barrages may see objections because of their visual presence above the water. A change in the tides natural curve may also trouble beach walkers but the reduction in sediment deposited on the beach would perhaps

balance this out.

2.5.3 Significant Impact Factor (SIF)

The SIF is a percentage value assigned to the resource at a particular site that could be extracted without resulting in a significant environmental impact. Take for example an arbitrary number of tidal stream devices in a tidal flow of constant velocity. Each device will extract energy from the flow proportional to its rated power and induce a degree of turbulence into the flow (McCombes, T. et al (2006)). This in turn could disturb sediment transport from nearby rivers and scour the seabed.

In terms of quantifiable tolerances for SIFs it varies from site to site but typical values fall in the range of 15-20%. This unfortunately significantly limits the amount of energy capture available for tidal stream devices therefore any advancements in the efficiencies of power production from tidal energy devices could increase appeal and commercial viability (Cowles, G. et al (2009)).

3 UNDERLYING THEORY

3.1 Fluid Mechanics

3.1.1 Basic Equations

One of the most important fundamental tools in fluid mechanics is the momentum equation and more specifically, its integral form. It is derived by applying Newton's second law, that states "the momentum at any point changes as a result of the forces acting on the fluid at that point," to a control volume. In Equation form this is given as:

$$\frac{d\vec{P}}{dt} = \vec{F} = \frac{\partial}{\partial t}\iiint \rho \vec{V}\, d(vol) + \iint \vec{V}\, \rho \vec{V} \cdot \overrightarrow{dA} \qquad (3.1)$$

This equation is often used to evaluate an unknown force given the velocity at the control surface. If used in conjunction with the control volume stresses, evaluated using Stoke's Hypothesis, the Momentum Integral Equation can be used to derive one of the most important results in the history of fluid mechanics: Navier Stokes Equations.

However, Navier Stokes Equations are notoriously hard to solve and the simpler integral moment of momentum is often used instead:

$$\vec{M} = \iint \vec{r} \times \vec{v}\, \rho \vec{V} \,.\, \overrightarrow{dA} \qquad (3.2)$$

These two important results of fluid mechanics can be used to derive the thrust and torque of a rotor such as those used on tidal turbines. This is developed in section 3.3 of this thesis.

3.1.2 The Boundary Layer

One phenomenon that is of great interest when considering the fluid flow around an object, such a turbine blade, is the boundary layer. This concept was introduced to the physics world by Ludwig Prandtl in 1904 and lends itself to the viscous properties of fluids such as air and water. It is in fact a thin layer of fluid at a submerged object's surface that forms due to the "no-slip condition." That is to say that skin friction causes the surrounding flow to rapidly slow to a point on the object's

surface where the fluid flow velocity is zero. Outside this layer the flow is often treated as inviscid but this may only be assumed in large Reynolds number flow fields.

Two types of boundary layer may exist at a solid object's surface: laminar and turbulent. The first of these is easily represented analytically and is present from the surface first approached by the free-stream flow (in the case of an aerofoil or turbine blade: the leading edge) up until a point determined by factors effecting transition location. Beyond this point transition occurs where laminar flow becomes turbulent and the boundary layer thickens. The governing factors over what portion of the boundary layer is laminar flow are predominantly Reynolds number, surface roughness and surface curvature.

The Reynolds number of a flow field is a dimensionless quantity that represents the ratio of the inertia force acting on a unit volume of fluid, as it is accelerated by a pressure gradient, and the viscous force on the same volume of fluid, which is resisting the motion of the fluid. The Reynolds number influences the viscous forces within the boundary layer and as it is increased, these forces weaken and vice versa (Burton, T. et al (2001)). Seeing as the boundary layer state is governed by viscous forces it is evident that for a range of low Reynolds numbers the flow will be laminar and for a range of high Reynolds numbers the flow will be turbulent. The range lying between these two ranges is known as the transition stage.

Surface roughness and curvature (or camber) effect the position of transition from laminar to turbulent boundary layer flow. An increase in surface roughness promotes transition and dependant on the Reynolds number of the flow at that point the turbulence created may propagate downstream or return to laminar flow. Similarly an increase in surface curvature promotes boundary layer separation.

3.2 The Betz Limit

Named after German aerodynamicist, Albert Betz, the Betz limit is “the maximum achievable value of power coefficient” and applies to all rotor-driven devices (REUK, 2006). The power coefficient is a dimensionless term often used as a performance indicator for rotors and is defined as:

$$C_P = \frac{Power}{\frac{1}{2}\rho U_\infty^3 A_d} \tag{3.3}$$

The power term in the numerator is defined as the power extracted from the air by the rotor when represented as an actuator disk. The actuator disk representation comes from actuator disk theory, which consists of a stream-tube analysis of an ideal rotor (see Figure 8). When mass conservation and momentum theory are applied to the stream-tube the velocities at the rotor and upstream and downstream of the rotor may be evaluated in terms of freestream velocity, U_∞ , and axial and tangential inflow factors, a and a'. This in turn allows the power and thrust of the device to be estimated through a process called the Blade Element Momentum Method (described in section 3.3). Using equation 3.3 the power can be non-dimensionalised by dividing the extracted power by the power available in the flow giving a value known as the power coefficient.

Betz Limit dictates that conceivably only a certain portion of the flow's energy can be extracted at any one time by an energy extraction device. This is conceptually understandable, since if the power coefficient were to equal one then the entirety of the flows energy would be extracted and the downstream flow would be stagnant. This value can be sought through differentiation of the power equation in terms of inflow factors (equation 3.4) and substitution of the result into equation 3.3.

$$P = 2\rho A U_\infty^3 \left(a - 2a^2 + a^3\right) \tag{3.4}$$

After differentiating with respect to inflow factor :

$$\frac{dP}{da} = 2\rho A U_\infty^3 \left(1 - 4a + 3a^2\right) \tag{3.5}$$

In order to satisfy the condition of maximum power the inflow factor must equal a third, giving the following equation for maximum power:

$$P_{max} = \frac{8}{27}\rho A U_\infty^3 \tag{3.6}$$

Substituting this into equation 3.3 gives a constant value of 0.593, which is consequently the Betz limit. In the context of an energy extraction device this implies that theoretically the maximum

amount of energy one device can extract from the flow is 59% of the total energy.

3.3 Blade Element Momentum Method

The Blade Element Momentum (BEM) Method is accredited to Glauert (1935) and couples momentum theory with local events taking place at the blades of a rotor, making it possible to calculate steady loads on the blades. These loads can then be used to calculate the thrust and power of the rotor for varying wind speeds, rotational speeds and pitch angles.

The method itself is relatively straightforward and easy to comprehend but requires iterative solutions and is therefore best implemented using computer software. To make implementation through computation simpler an algorithm is outlined in this section. Before this algorithm can be described the underlying theory and equations are put across.

The BEM method relies on the discretization of the streamtube control volume surrounding the turbine rotor into N 2-D annular elements of height dr, which have lateral boundaries that are treated as streamlines and therefore there is no cross flow. Consider a Control Volume (C.V.) containing a turbine of cross-sectional area A_1. The upstream flow and downstream flow outside of the streamtube have freestream velocity U_∞, the flow at the rotor has velocity u_1, and the flow downstream of the rotor has velocity u_2.

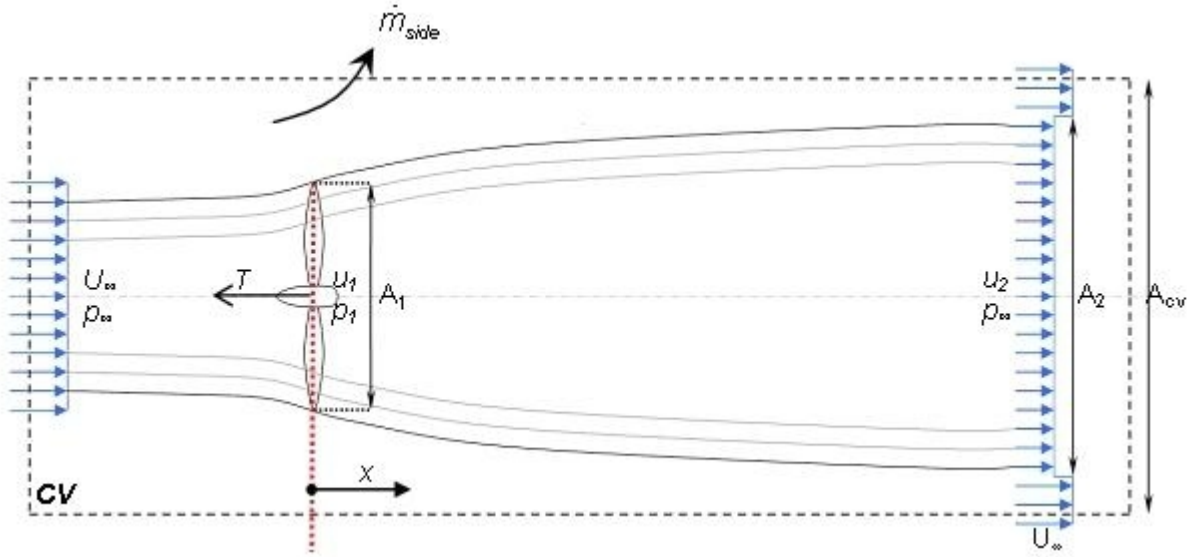

Figure 8: *Control Volume Containing Streamtube Around Rotor*

The following assumptions are made for the annular elements (Burton, T et al (2001)):

- That there is no radial dependency and therefore anything that happens at one element does not carry over to adjacent elements.
- That the force from the blades on the surrounding flow is constant in each annular element. This corresponds to a rotor with an infinite number of blades.

A further assumption is made that the forces on a blade element can be calculated by means of 2-D aerofoil characteristics using angle of attack values determined from the incident resultant velocity in the cross-sectional plane of the element. With this said, velocities in the spanwise direction and three dimensional effects may be ignored (Hansen, M.O.L. (2008)).

The first step in the BEM method is to apply the integral form of the axial momentum equation to the above C.V. to give an expression for the thrust, T, produced by the turbine.

$$\frac{\partial}{\partial t}\iiint \rho u(x,y,z)\,dxdydz + \iint u(\mathrm{x,y,z})\rho \mathrm{V}\cdot\vec{d}\,A = \vec{F}_{ext} + \vec{F}_{press} \tag{3.7}$$

The C.V. experiences equal pressure on it's end planes and the force is over an equal area therefore the last force term in Equation 3.7 can be assumed to be zero. The only external force is then the thrust and through momentum conservation expressions for the mass flow rate of flow leaving through the side of the C.V. and for the C.V. area A_2 may be obtained.

$$T=\rho uA\left(U_\infty - u_2\right) = \dot{m}\left(U_\infty - u_2\right)$$
$$so\ dT=\left(U_\infty - u_2\right) d\dot{m} = 2\pi r\rho u\left(U_\infty - u_2\right)dr \tag{3.8}$$

In a similar manner the Integral Moment of Momentum Equation can be applied to the same C.V. to obtain an expression for the torque, dM, on the annular element. For the aforementioned C.V. It is assumed that the rotational velocity upstream is zero and that in the wake it is Uθ:

$$dM=rU_\theta d\dot{m} = 2\pi r^2 \rho u U_\theta dr \tag{3.9}$$

Now substituting into the thrust equation for $u_2=(1-2\mathrm{a})U_\infty$:

$$dT = 4\pi r \rho U_{\infty}^{2} a(1-a)\,dr \tag{3.10}$$

Similarly substituting for Uθ=2a'ωr in the torque equation:

$$dM = 4\pi r^{3} \rho U_{\infty} \omega (1-a) a' dr \tag{3.11}$$

In order to solve for a and a' we require another equation for thrust and another for torque. This is achieved through analysing the local flow geometry around the blade. Consider a turbine with N blades of tip radius R, each with a chord c and set pitch angle θ. Let:

- both chord and pitch may vary along the blade span.
- the blades be rotating with angular velocity ω.
- Let freestream wind velocity be U_{∞}.

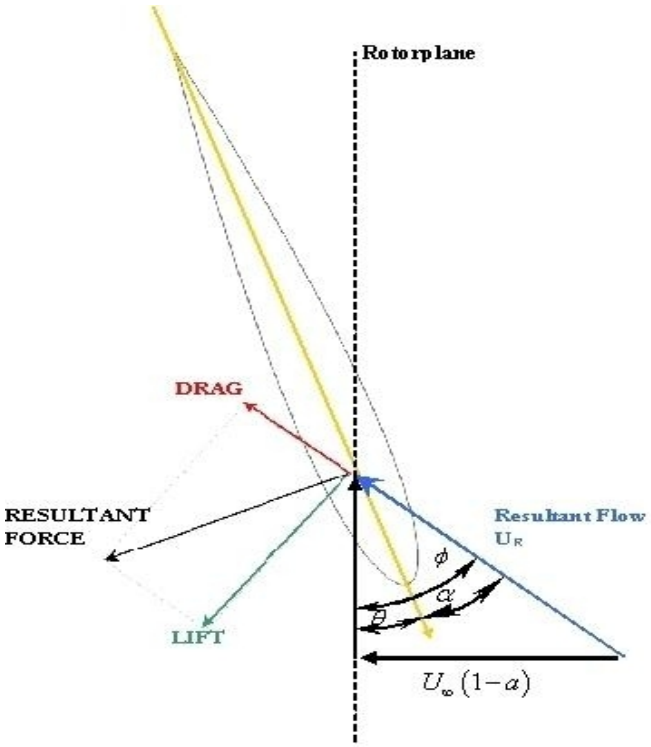

Figure 9: *Blade Element Forces and Velocities*

Where the resultant velocity at the blade, UR, is given by:

$$U_R = \sqrt{U_{\infty}(1-a)^2 + \Omega^2 r^2 (1+a')^2} \tag{3.12}$$

This resultant velocity acts at an angle φ to the flow, which is hence designated the flow angle, as shown in Figure 9. The flow angle can then be expressed in terms of the sine and cosine of this angle.

$$U_R = \frac{U_\infty (1-a)}{\sin\varphi} = \frac{\Omega r (1+a')}{\cos\varphi} \tag{3.13}$$

These two trigonometric functions can be combined to give a single expression in terms of the tangent of the flow angle:

$$\tan\varphi = \frac{(1-a)U_\infty}{(1+a')\omega r} \tag{3.14}$$

From this the flow angle may be evaluated and hence if the pitch angle is known, simple angle subtraction allows the angle of attack, α, to be calculated:

$$\alpha = \varphi - \theta \tag{3.15}$$

where the local pitch, θ, is given by: $\theta = \theta_p + \beta$ (3.16)

The standard aerodynamic expressions for lift and drag yield:

$$L = \frac{1}{2}\rho U_{rel}^2 c C_l dr \quad D = \frac{1}{2}\rho U_{rel}^2 c C_d r dr \tag{3.17}$$

Now the lift and drag projected into normal and tangential directions give:

$$F_N = L\cos\varphi + D\sin\varphi \tag{3.18}$$

$$F_T = L\sin\varphi - D\cos\varphi \tag{3.19}$$

Similarly, in terms of lift and drag coefficients, C_l and C_d:

$$C_N = \frac{F_N}{\frac{1}{2}\rho U_{rel^2} c} \quad C_T = \frac{F_T}{\frac{1}{2}\rho U_{rel^2} c} \tag{3.20}$$

Since Fy and Fx are forces per unit length, the thrust, given by the normal force, and the torque, dT and dM on the C.V. With thickness dr are given by the following expressions:

$$dT=BF_N\,dr \quad dM=rBF_T\,dr \tag{3.21}$$

Now, substituting for F_N and F_T in terms of C_N and C_T and then for U_R from equation 3.13.

$$dT=\frac{1}{2}\rho B\left(\frac{U_\infty(1-a)}{\sin\varphi}\right)^2 cC_N \tag{3.22}$$

$$dM=\frac{1}{2}\rho B\left(\frac{U_\infty(1-a)}{\sin\varphi}\cdot\frac{\omega r(1+a')}{\cos\varphi}\right)cC_T \tag{3.23}$$

Equating equations 3.10 and 3.11 with 3.22 and 3.23 & rearranging gives explicit expressions for a and a':

$$a=\frac{1}{\frac{4\sin^2\varphi}{\sigma C_N}+1} \quad a'=\frac{1}{\frac{4\sin\varphi\cos\varphi}{\sigma C_T}-1} \tag{3.24}$$

Where the local solidity is defined as: $\sigma(r)=\frac{c(r)B}{2\pi r}$ (3.25)

These two values allow the local loads on blade segments to be calculated and therefore complete the algorithm required to implement BEM method in a computer program. In order to achieve the optimum degree of accuracy from the BEM method two corrections must first be applied.

3.3.1 Prandtl's Tip Loss Factor

This correction is required to compensate for the second of the initial assumptions made at the beginning of section 1.2.3 that assumes the turbine rotor consists of an infinite amount of blades. This correction is required because of the difference in wake vortex systems between infinite and finite bladed rotors. Prandtl derived a correction factor F to equations 3.10 and 3.11:

$$dT=4\pi r\rho U_\infty^2 a(1-a)F dr \tag{3.26}$$

$$dM=4\pi r^3\rho U_\infty\omega(1-a)a'F dr \tag{3.27}$$

Where $F=\frac{2}{\pi}\cos^{-1}\left(e^{-f}\right)$ & $f=\frac{B}{2}\frac{R-r}{r\sin\varphi}$ (3.28)

This correction yields the following equations for a and a':

$$a=\frac{1}{\frac{4\mathrm{Fsin}^2\varphi}{\sigma C_N}+1} \quad a'=\frac{1}{\frac{4\mathrm{Fsin}\varphi\cos\varphi}{\sigma C_T}-1} \tag{3.29}$$

3.3.2 Glauert's Correction for High Values of a

When the axial induction factor, a, exceeds values of approximately 0.4 the simple momentum theory breaks down due to a prediction of a flow reversal in the wake. This is an impossible outcome and what actually occurs is a transition form laminar to turbulent flow. To account for this breakdown in the BEM method different empirical relations between thrust coefficient, C_T, and axial induction factor, a, were developed:

$$C_T=\begin{Bmatrix} 4a(1-a)F\left[a\le\frac{1}{3}\right] \\ 4a\left(1-\frac{1}{4}(5-3a)a\right)F\left[a>\frac{1}{3}\right] \end{Bmatrix} \tag{3.30}$$

$$C_T=\begin{Bmatrix} 4a(1-a)F\left[a\le a_c\right] \\ 4\left(a_{c^2}+\left(1-2\mathrm{a}_c\right)a\right)F\left[a>a_c\right] \end{Bmatrix} \tag{3.31}$$

Figure 10 illustrates these two sets of equations and compares them to the standard momentum theory results for a Prandtl correction factor of one.

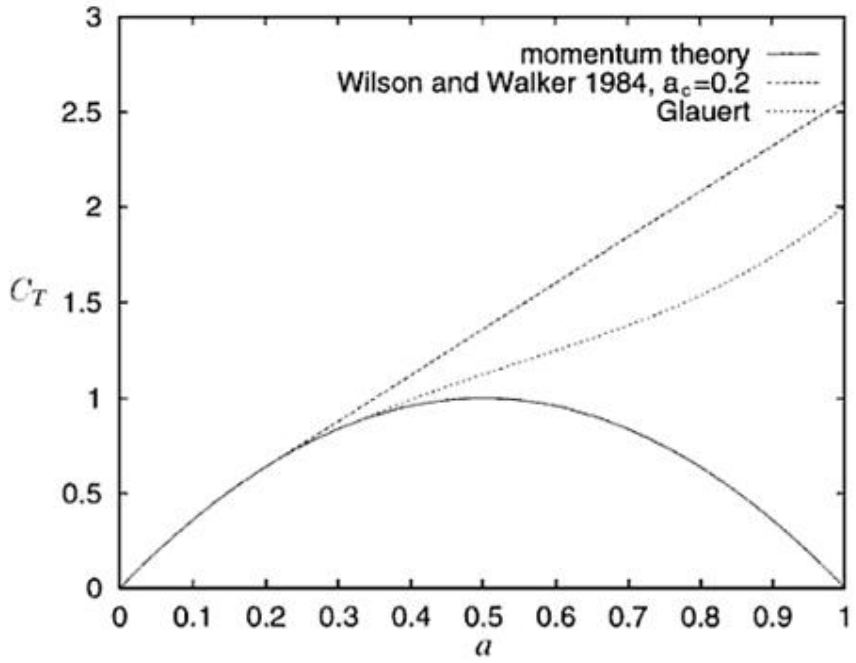

Figure 10*: Comparison of Momentum Theory Results with F=1*

From local aerodynamics the thrust, dT, is given by equation 3.22 and by definition CT is given by:

$$C_T = \frac{dT}{\frac{1}{2}\rho U_\infty^2 2\pi r dr} \tag{3.32}$$

Combining the two equations:

$$C_T = \frac{(1-a)^2 \sigma C_N}{\sin^2 \varphi} \tag{3.33}$$

Now, if a>ac, this expression can be equated with the emperical expression (2nd of equation 3.30) and rearranged for a to give:

$$a = \frac{1}{2}\left[2 + K(1-2a_c) - \sqrt{(K(1-2a_c)+2)^2 + 4(Ka_c^2 - 1)}\right] \tag{3.34}$$

where $K = \frac{4F\sin^2\varphi}{\sigma C_N}$ (3.35)

3.3.3 BEM Method Algorithm

With these two correction's to the BEM method explained the algorithm for computational implementation of the BEM method can now be described:

Step	Code
1	**Initialise *a* and *a'*, typically *a*=*a'*=0**
2	**Compute flow angle φ using equation 3.14**
3	**Compute the local angle of attack using equation 3.15**
4	**Compute Prandtl's Correction Factor F using equation 3.28**
5	**Use look-up tables to find CL(α) & CD(α).**
6	**Compute C_N and C_T using equation 3.20**
7	**Calculate *a* and *a'*:** − **If $a \leq a_c$ use equation 3.29** − **If $a \geq a_c$ use equation a 3.34** − **For *a'* use equation 3.29**
8	**Ensure *a* and *a'* are within decided tolerance otherwise return to step 2.**
9	**Compute local loads on blade segments.**

3.3.4 Computing Thrust, Power and Root Bending Moment

Once the BEM method algorithm has been applied to all the C.V.s making up the entire rotor the tangential and normal load distributions are known and therefore the global parameters such as mechanical power, thrust and root bending moments can be evaluated.

In order to evaluate the tangential force per unit length, F_{Ti}, is known for each segment at radius, r_i, and linear variation between r_i and r_{i+1} is assumed. F_T between r_i and r_{i+1} is thus:

$$F_T = \left\{ \frac{F_{T,i+1} - F_{T,i}}{r_{i+1} - r_i} \right\} r + \left\{ \frac{F_{T,i} r_{i+1} - F_{T,i+1} r_i}{r_{i+1} - r_i} \right\} \tag{3.36}$$

The torque dM for an infinitesimal part of the blade, dr, is given by:

$$dM = rF_T\,dr \tag{3.37}$$

It makes sense then that the total shaft torque is the sum of all the contributions from the linear tangential load variation between r_i and r_{i+1} along one blade multiplied by the number of blades.

$$M_{TOT} = B\sum_{1}^{N-1}\left[\frac{1}{3}\left\{\frac{F_{T,i+1}-F_{T,i}}{r_{i+1}-r_i}\right\}\left(r_{i+1}^3-r_i^3\right) + \frac{1}{2}\left\{\frac{F_{T,i}r_{i+1}-F_{T,i+1}r_i}{r_{i+1}-r_i}\right\}\left(r_{i+1}^2-r_i^2\right)\right] \tag{3.38}$$

It follows from this that $P_{shaft} = \omega M_{TOT}$. (3.39)

4 CONTRA-ROTATING TURBINES

4.1 A Brief History of Contra-rotating Rotors

The concept of contra-rotating blades consists of two coaxial rotors of opposite rotational senses and has been around since the early 19th century. The first contra-rotating devices were manufactured for use on steam boats for their inherent characteristic of torque cancellation and therefore an improvement in lateral stability of the craft being propelled. This principle was also applicable to the more common use of contra-rotating propellers on torpedoes (Breslin, J.P. & Andersen, P (1996)).

With uses of contra-rotating technology being used in marine applications thus far it was the First World War that saw an expanding of this technology to aircraft applications. However, it wasn't until the Second World War and the invention of the Spitfire 24 that the technology was utilised for it's attractive features of torque cancellation and increased efficiency. Consequently problems occurring at take-off incurred due to an increased torque saw the applications of such propellers kept to a minimum.

The invention of the jet engine by Sir Frank Whittle in 1930 opened a new window of opportunity for the use of contra-rotating blades. Again, it wasn't until much later in the century that this opportunity was seen by industrialists. It was in the manufacture of turbines and compressors for jet engine applications that the use of contra-rotating blades was seen to be beneficial. The compressor and turbine stages used in engines are made up of multiple stages, the amount of which is dependant upon the desired pressure ratios. With the use of contra-rotating blade pairs to compress and expand the air the requirement for stator stages is eradicated and weight is therefore saved. The increase in efficiency over a single rotor stage also means that fewer stages are required for a given pressure ratio and hence space savings can be made (Reaction Engines limited (2006)).

The most recent, and perhaps most relevant, application of contra-rotating rotors is in the renewables sector; in particular the wind turbine industry. The U.S. led the research into this with the California Energy Commission carrying out a feasibility analysis into a grid-connected 50-100kW wind turbine system in 2003 (California Energy Commission (2003)). Following this study it was concluded that up to 40% more energy could be extracted from the free-stream than a conventional single rotor wind turbine. However, feasibility studies would need to be carried out to

ascertain whether the increase in mechanical complexity would be outweighed by this improvement in energy capture.

4.2 Advantages of a Contra-rotating Turbine over Single Rotor Turbines

A few of the advantages of a contra-rotating turbine were mentioned in the previous section and now this section aims to describe the underlying reasons behind these advantages and how they are beneficial to the manufacturer. The main advantages of a contra-rotating turbine are:

- Negligible reaction torque on the supporting structure
- Counter-acting wake swirls from adjacent rotors.
- High relative rotational speeds.

The first of these advantages stems from the fact that the rotors rotate in opposite directions and therefore the reaction torques produced by both rotors work against each other. The benefits of this characteristic are that there is a reduction in structural fatigue and no energy is wasted trying to negate the reaction torque through other means.

The outcome of the second bullet-point is that there is a different wake structure created by the turbine, which trails behind the rotor. If this wake structure were to be reduced it could consequently reduce the environmental impact of shallow water devices due to seabed degradation in the vicinity of the turbine. A secondary benefit is that tidal stream devices in close proximity to each other, as in tidal farms, would not see as much disruption in performance due to turbulent wake interference.

The third and final advantage is that high relative rotational speeds are achieved, which in turn produces a greater power output. This characteristic also has the added benefit that it reduces the need for a gear-train assembly.

4.3 ESRU's CoRMaT Design

The University of Strathclyde's Energy Systems Research Unit (ESRU) are currently working on the development of a Contra-rotating Marine Turbine (CoRMaT), mentioned in section 2.4.2. The turbine has been through prototype testing stages at $1/30^{th}$ and $1/10^{th}$ scale conditions. The results of these were promising in terms of power output and structural loading.

The basic design of the CoRMaT device follows a design philosophy that aims to minimise capital cost by exploiting the advantages outlined in the previous section.

4.3.1 CoRMaT Design Process

In order to design the contra-rotating turbine some preliminary analysis was required to ascertain the optimum geometry of the downstream rotor given the upstream rotor geometry. This was achieved using an adaptation of BEMM (Grant, A.D. (2007)) extended to apply to a contra-rotating turbine in which the tangential and axial flow induction factors were used as inputs to the second rotor. These were obtained by the method described in section 3.3 and then used to calculate the characteristics of the second rotor.

The CoRMaT device currently uses the NREL S814 blade section on both rotors and consist of an upstream rotor of three blades and downstream rotor of four. In order to achieve the design condition of zero net torque for the CoRMaT device it was found from the BEMM that the tip speed ratios of upstream and downstream rotors should be 3 and 2.875 respectively. This constituted to an axial thrust distribution of 51/49 percent.

The testing of the two scaled prototype models previously mentioned was then carried out under these conditions in the university's tow-tank and non-dimensionalised results of power coefficient against tip speed ratio produced. These could then be compared to the predicted result to verify the BEMM prediction method. During these tests a hydraulically actuated disk brake was used to control rotational speeds of the rotors.

4.3.2 Some Results from the CoRMaT Prototype Testing

$1/30^{th}$ prototype testing at different rotor spacings and blade pitch angles yielded some interesting results in terms of non-dimensional characteristics: tip speed ratio and power coefficient. The two graphs below display these results, with the graph on the left displaying results for zero pitch angle and two different rotor spacings against the predicted result. The graph on the right displays the same three trends but with a blade pitch angle of two degrees on both rotors. In both graphs it can be seen that the minimum rotor spacing results follow the prediction trend closely, therefore

verifying the prediction method used.

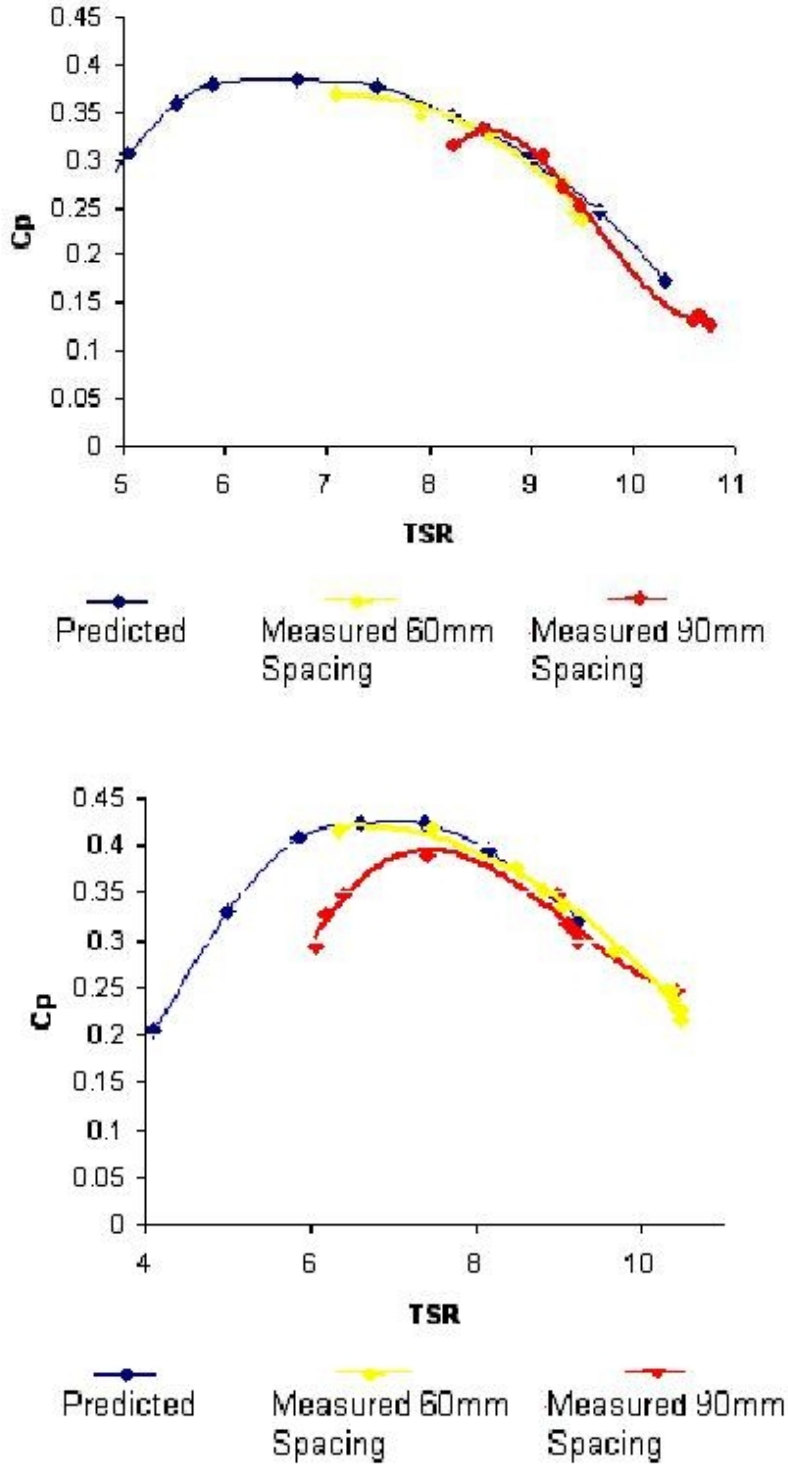

Figure 9: *Tip speed ratio vs. Power coefficient for different rotor spacing and blade pitch angles* (Clarke J.A. et al (2007)).

It was from these results and others produced through computational fluid dynamics (CFD) and Finite Element Analysis (FEA) that the second, larger, prototype was designed and built. This 1/10th scale prototype has now undergone sea trials in the Holy Loch (Clyde approaches). This was achieved by the turbine being towed behind a fishing vessel at 1.5 m/s. Through this sea trial, limitations of the hydraulic system used to control the disk brakes were recognised but power curves were close to predictions. Also, through analysis of dynamic loading on the hub it was noticed that edgewise loading was reduced when both rotors were rotating in comparison to just one, therefore justifying the need for a second rotor. This reduction in loading is depicted in figure 10, where the graph on the left is both rotors rotating and the right-hand graph shows recorded loadings when the upstream rotor was stopped.

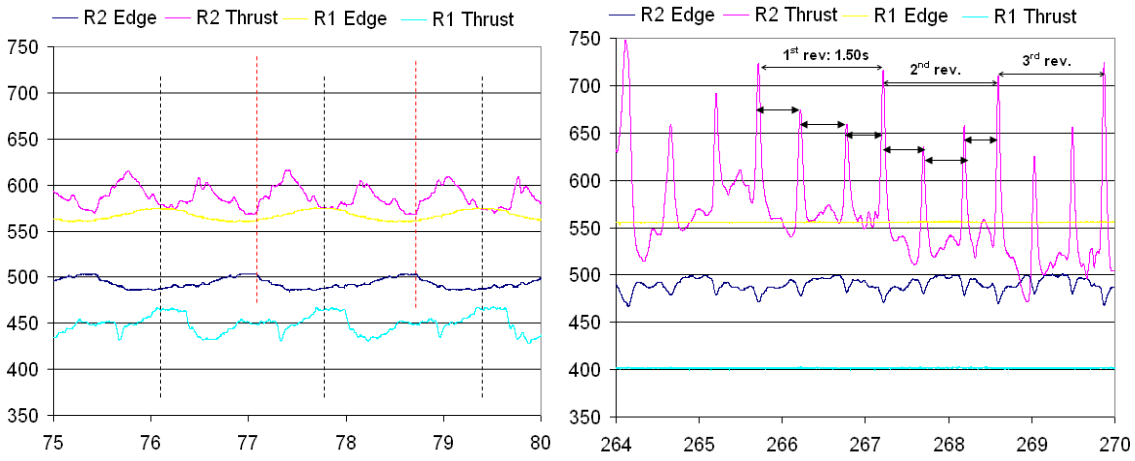

Figure 10: *Blade Thrust and Edgwise Loadings (arbitrary units) over time* (Clarke J.A. et al(2007))

5 HYDROFOIL SECTION SELECTION FOR A CONTRA-ROTATING TIDAL TURBINE

5.1 Criteria for Tidal Stream Turbine Blade Design

When choosing the blade profile for a tidal turbine there are criteria that are beneficial, in terms of power output, efficiency and life-time, for the manufacturer to meet. These criteria may differ slightly from design to design but by in large the objectives of different designs are similar in principle.

The Lift and Drag characteristics of a blade are obviously important parameters inherent in the design of a blade profile. It is beneficial for a blade operating on a turbine to maintain a relatively high lift coefficient at high angles of incidence because of the circular plane they operate in. This therefore leaves them highly susceptible to stalling and consequently a loss in power output. It is evident then that hydrodynamic considerations lead to important criteria when choosing blade sections. These criteria are often along the lines of:

- High C_{Lmax} along the span of the blade to delay stall.
- Corresponding low drag coefficient at C_{Lmax}.
- A C_{Lmax} value that is insensitive to surface roughness.
- A high post-stall C_{Lmax} value

Along with hydrodynamic performance, another important characteristic that a turbine blade must exhibit is resistance to loads that it experiences from the fluid medium it is in. In the case of a tidal turbine device this is obviously water. Water, as previously mentioned, is over eight hundred times denser than air and therefore the forces and moments experienced by a tidal turbine are quite different from those experienced by a wind turbine. In the case of wind turbines centrifugal loads dominate therefore restricting bending and dictating the structural demands of the rotor hub. Conversely, for tidal turbines, the increase in working fluid density and low relative free-stream velocities mean that the dominant loads are bending moments (Marsh, G. (2004)). The lower free-stream velocity of tidal flows and the limited diameter of the turbine rotor mean that centrifugal forces are much lower than those of wind turbines. These low centrifugal forces offer little resistance against bending, hence the need for structural improvements to ensure a feasible lifetime. These structural improvements can be in the form of materials or an increase in hydrofoil thickness for example.

Though this resistance to bending is obviously an important issue when considering the lifetime of tidal turbines it is mainly considered with three-dimensional hydrodynamic effects and therefore out with the scope of this thesis. For this reason this chapter will be primarily concerned with the hydrodynamic characteristics of 2-D blade sections with a small section on material selection and geometric considerations.

5.2 Material Selection and Geometric Considerations

Material Selection, as mentioned in the previous section, is of great importance when designing a tidal turbine because of the unusually high bending moments experienced by the blades on these devices. Initial designs of the Seaflow device were seen to utilise steel blades because of the stiff properties of this material (Marsh (2004)). However, the corrosive nature of seawater soon saw steel to be replaced by a composite material. In this case the composite was a reinforced plastic-based material. One advantage of using composite materials is their orthotropic property, gained by orthogonally orientated laminate layers. This means that they do not have an axis about which an applied force or moment will cause more damage than it would if applied about any other axis. The unfortunate disadvantage of composites is the fact that they are currently expensive and therefore have a profound impact on the economics of such a system. One of the stronger composites available today is carbon-fibre, which consequently is one of the most expensive available. This implies a compromise has to be made in the form of a trade off between capital cost and structural integrity. In the case of Seaflow a carbon-fibre main spar was encased in a glass-fibre envelope and carbon-reinforced ribs connected the two. This design meant that costs were saved and a robust, stiff blade was constructed. A similar blade design was used in the successor, SeaGen, which was installed in Strangford Lough in 2008 but unfortunately blade structural problems were encountered.

Another factor that strongly affects the forces experienced by a blade and its stiffness is its geometry. The geometry of existing tidal turbine blades is predominantly based upon wind turbine designs. The main difference being that tidal turbine blades tend to be shorter and therefore have a smaller aspect ratio. This has a profound effect on the stiffness of the blade and on the power output of the device. With respect to the aforementioned blade structural problems encountered by the Seagen design, an alternative solution could be changing the blade geometry instead of

materials. This would obviously be the cheaper option in terms of R&D and capital costs but a drop in power output may be observed. One such solution would be to thicken the blade in order to increase its rigidity. The implications of this would be an increase in maximum lift coefficient but also an increase in overall drag coefficient.

5.3 Hydrodynamic Performance Analysis of some commonly used Blade sections in Renewable Power Generation Devices.

This section contains an analysis of two NREL aerofoil sections and two NACA aerofoil sections in terms of general 2-D hydrodynamic performance and in particular lift and drag characteristics and post-stall behaviour. The one, from each institute, with the most desirable characteristics was then included in the BEMM computational analysis described in chapter 6. This analysis was carried out with the aid of Javafoil, which was used to show Cp distributions and lift coefficients at different angles of attack and Reynolds numbers as well as drag polars. This allowed a prediction verification of post-stall behaviour in terms of boundary layer separation and severity of drop in lift coefficient and rise in drag coefficient. Javafoil uses a panel method code and integral method to carry out potential flow and boundary layer analyses respectively. This application was chosen over potential alternatives, such as X-FOIL, because of its user friendly interface and easy to use section geometry plotting feature. It should be mentioned at this point that for all analysis done in this chapter it was assumed that flow was inviscid and incompressible and all section characteristics are 2-D, with no consideration of radial flow.

5.3.1 An Introduction to NREL Section Families Used In Turbine Design

The National Renewable Energy Laboratory (NREL) began a joint pursuit with Airfoils, Incorporated in 1984 to design aerofoils specifically for Horizontal Axis Wind Turbines (HAWTs). The design philosophy behind the nine existing families is one aimed at increasing annual energy production by reducing effects of surface roughness on maximum lift coefficient. This was done while accommodating the needs of rotors of stall-regulated, variable pitch and variable RPM varieties. With respect to the CoRMaTs variable RPM design the NREL airfoils are advantageous because of their high C_{Lmax} values from root to tip lending to low blade solidity. NREL claim an additional 8-10% in energy capture is achieved for variable RPM devices when using their aerofoils but this has only been verified through testing for stall-regulated systems (Tangler, J.L. & Somers,

D.M. (1995)). The numbering system adopted by NREL is purely chronological and spans from the S801, created in 1984, to the S828, created in 1995. In addition to this numbering system is a thickness designation with the simple labels of "thick", corresponding to any aerofoil within the 11-15% thickness range, and "thin", which corresponds to any aerofoil falling in to the 16-26% range. Some potential combinations of these aerofoils sorted by the magnitude of power generation required are outlined in Figure 11 below.

Blade Length (meters)	Generator (kW)	Thickness Category	Airfoil Family (root----------tip)			
1-5	2-20	thick		S823		S822
5-10	20-150	thin		S804	S801#	S803#
5-10	20-150	thin	S808	S807	**S805A**	S806A
5-10	20-150	thick		S821	S819	S820
10-15	150-400	thick	S815	**S814**	**S809**	S810
10-15	150-400	thick	S815	**S814**	S812	S813
10-15	150-400	thick	S815	**S814**	S825#	S826#
15-25	400-1000	thick		S818	S816	S817
15-25	400-1000	thick		S818	S827	S828

shaded - - - - - Ohio State, Univ. of Ill.
bold numbers - - - Delft tested
crosshatch - - - - - - high $c_{L\max}$ tip airfoils, S825 LTPT test

Figure 11: *Combinations of NREL airfoil families sorted by generator size* (Tangler, J.L. & Somers, D.M. (1995))

Two NREL aerofoil sections of interest when considering blades for use on a tidal turbine are the S814 and S815 sections. These two sections are designed to be used on HAWTs with blades within the range 10-15 metres (as depicted in Figure 11) and replaced the S811 family because of their superior insensitivity to roughness. The performance characteristics of these aerofoils related to application on a tidal stream device are discussed in the following two sections.

5.3.2 Hydrodynamic Performance of NREL's S814 Section

The S814 aerofoil section is 24% thick and is intended for use up to a blade radial station of 0.4 of a wind turbine. When utilised for this purpose its design objectives were to have a maximum lift coefficient (C_{Lmax}) of 1.3 at a Reynolds number of 1,500,000 and to maintain low profile-drag coefficient values for the lift coefficient range of 0.6-1.2, which correspond to the design radial station of 0.4. This C_{Lmax} value has the added design constraint that it doesn't decrease with transition occurring near the leading edge on upper and lower surfaces. The appearance of the S814 section once recreated in JavaFoil using co-ordinates taken from Somers (2004) is shown in Figure 12.

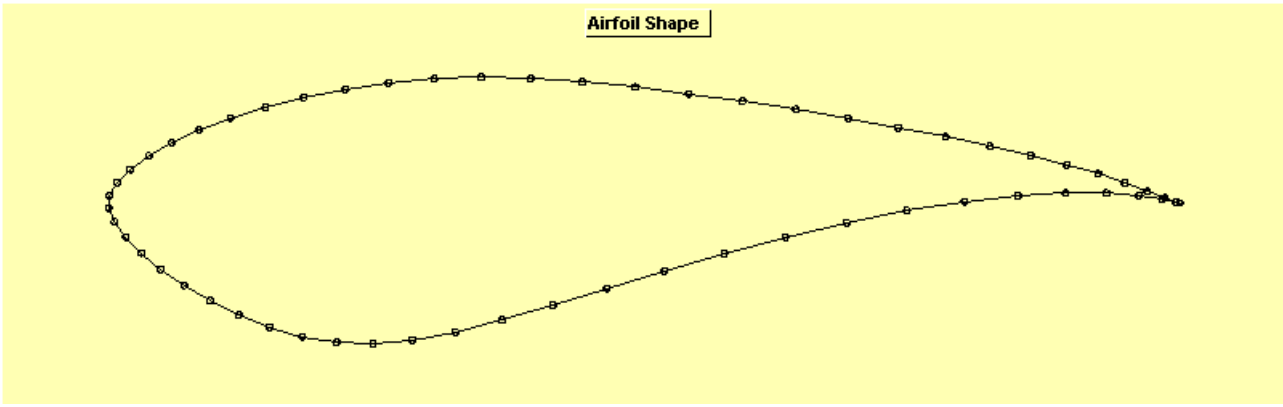

Figure 12: *S814 Section shape created in JavaFoil*

The section lift and drag characteristics over a 360 degree rotation were ascertained with the use of JavaFoil and data exported to Excel for analysis. This analysis was done for three scenarios of differing surface roughness and transition location. The first of these scenarios consisted of smooth surfaces on upper and lower surfaces and the second, available in JavaFoil, simulated roughness effects such as bugs and dirt on upper and lower surfaces. The final scenario, taken from the NREL's subcontractor report (Somers, D.M. (2004)), consisted of fixed transition locations on upper and lower surfaces at 2% chord and 10% chord respectively. The lift curves shown in Figure 13 clearly show coincident C_{lmax} values for both high and low Reynolds number flow that are insensitive to roughness effects. The trends of the three scenarios are remarkably similar, with a small discrepancy due to difference in transition location post-stall. This small discrepancy suggests that post-stall performance is improved when transition location is fixed near the leading

edge, with smoother decrease in lift coefficient after stall and a higher C_{lmax} value. The two trends representing smooth and rough blade surfaces exhibit no noticeable difference in lift characteristics over the Reynolds number range of 100,000 to 3,000,000. It was also observed that at a Reynolds number of 100,000 both trends display sharp stall characteristics at 14 degrees then shortly after, at approximately 30 degrees, recover and continue to follow the trend of the lift curve of the section with transition fixed at 2% and 10 % on upper and lower surfaces respectively. In fact, past 30 degrees, no Reynolds numbers effects are observed on lift coefficient for all three transition scenarios.

The symmetric appearance of Figure 13 illustrates that over a 360 degree rotation four peaks of lift coefficient occur, with a lesser peak occurring at an angle of attack of 157 degrees. This value of 1.65 is the same for all Reynolds numbers. The C_{lmax} of the S814 does however vary with Reynolds number and ranges from 1.71 for rough and smooth surface finish and 1.74 for transition location fixed near the leading edge to 1.89 for all three scenarios. It should be mentioned her that a true line of symmetry exists about the alpha axis and the plots shown in Figure 13 are mirrored about this axis over a 360 degree rotation.

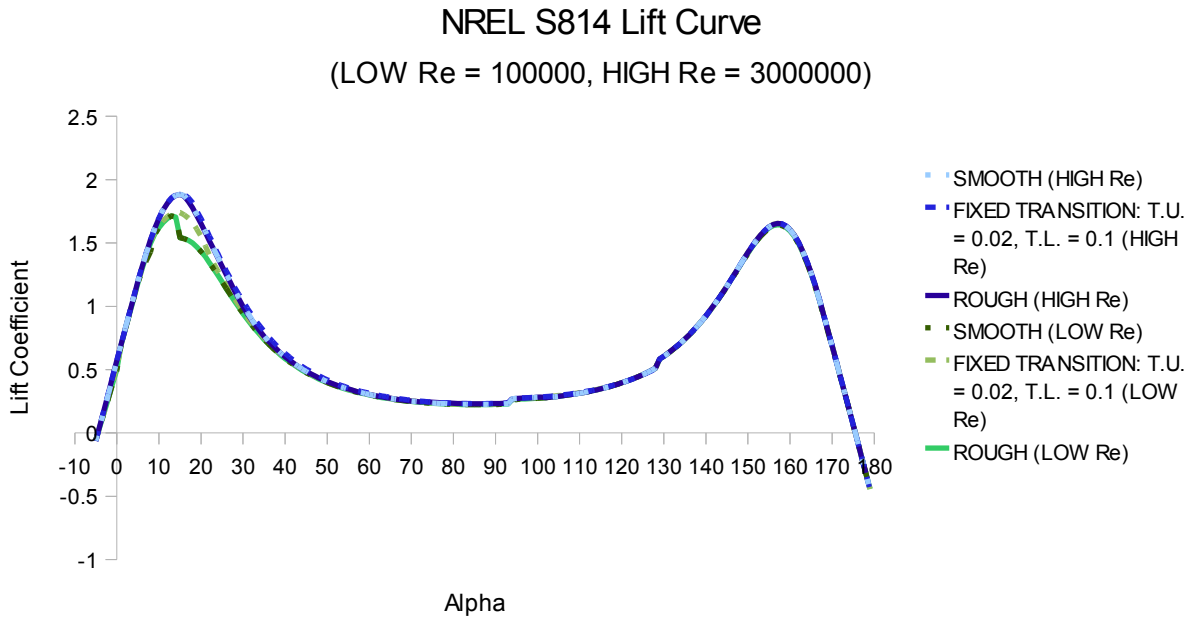

Figure 13: *S814 Lift Curve Plotted over alpha range -5<alpha<179 at low and high Reynolds numbers.*

The S814 drag polars produced using JavaFoil for the three transition conditions previously mentioned are shown in Figure 14 and show a clear difference in drag characteristics between low and high Reynold's number flow conditions. A sharp drag rise occurs when the lift coefficient approaches a minimum of 0.22 between peaks at around an angle of attack of 90 degrees. The maximum drag coefficient observed at this point is 6.73, which is an order of magnitude above a desirable value for drag coefficient. However, this may not be representative of the real-time performance of the S814 section on a tidal turbine. Figure 13 & Figure 14 exhibit a decrease in lift coefficient and increase in drag coefficient post-stall as would be expected due to boundary-layer separation occurring at stall. Consequently, the panel method used predicts a continuation of this behaviour up until an angle of attack of 90 degrees and therefore resulting in an unnaturally high drag coefficient.

With this said, the design objective for this NREL section of maintaining a low profile-drag coefficient over the lift coefficient range 0.6-1.2 could be claimed was achieved. Figure 14 clearly shows that the overall drag coefficient remains below 1 for this drag range and up until stall does not exceed 0.07 for low Reynolds number flow or 0.03 for high Reynolds number flow. These values are more desirable when talking in terms of drag coefficient but do not, however, take into account roughness effects.

As might be expected with any blade section an increase in drag coefficient can be observed from a subsequent increase in surface roughness. This could be illustrated for the S814 by observing the difference in drag coefficient at C_{lmax} between the three different transition scenarios for low and high and Reynolds number. In low Reynolds number flow the drag coefficient at C_{lmax} ranges from 0.063 to 0.093 due to surface roughness. The same range for high Reynolds number flow is 0.028 to 0.046.

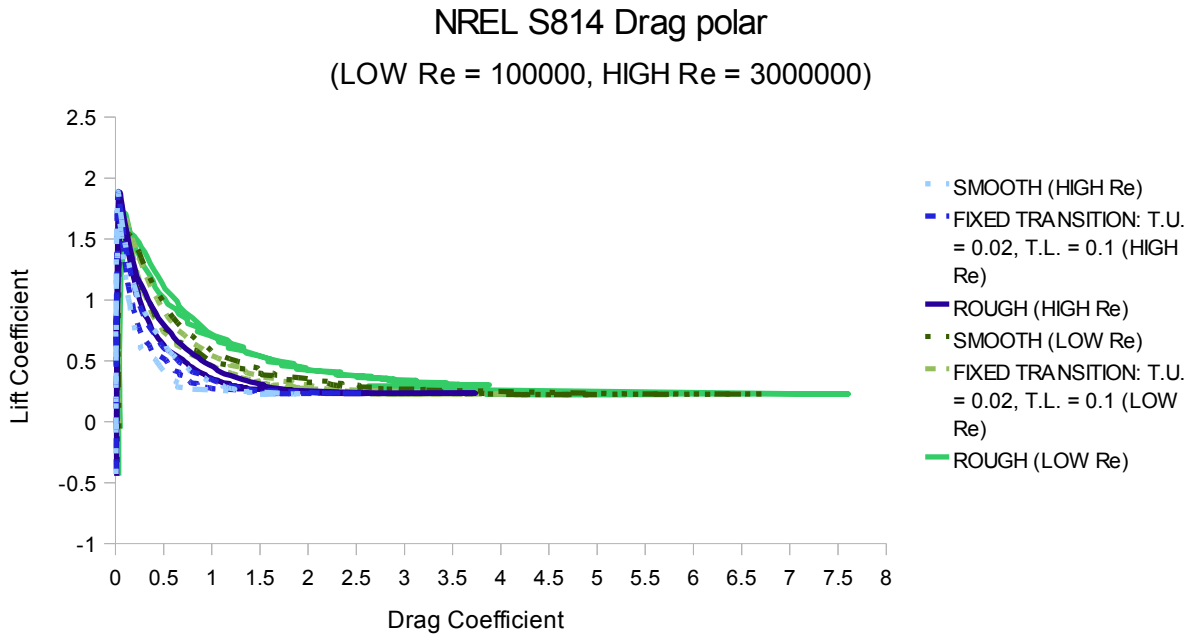

Figure 14: *S814 drag polar plotted over alpha range -5<alpha<179 at a low and high Reynolds number.*

Reynolds number effects on the S814 drag polar are significant with peak drag coefficient almost halving when Reynolds number was increased from one hundred thousand to three million. The value of the minimum drag coefficient also dropped considerably with increase in Reynolds number. At the low Reynolds number minimum drag coefficient varied from 0.02 to 0.033 with changes in surface roughness and transition location, which dropped to 0.003 to 0.006 in high Reynolds number flow.

5.3.3 Hydrodynamic Performance of NREL's S815 Section

The S815 is the thicker of the two NREL sections with a thickness of 26% chord and is intended for use up to a blade radial station of 0.3 of a wind turbine. It has a lower design C_{lmax} than that of the S814 of 1.1 corresponding to a lower design Reynolds number of 1,200,000. The S815 has the same design constraint of a C_{lmax} value that doesn't decrease with transition occurring near the leading edge. The range of lift coefficient values at which low profile-drag coefficient is to be maintained is 0.4-1.0. The appearance of the S815 section once recreated in JavaFoil using co-ordinates taken from Somers (2004) is shown in Figure 15.

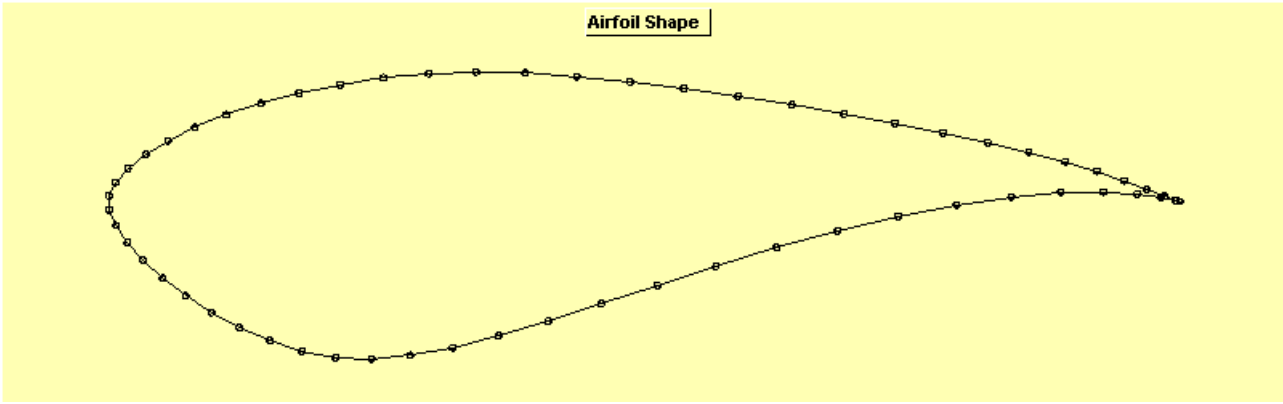

Figure 15: *S815 section shape created in JavaFoil*

The S815 lift curve shown in Figure 16, like the S814, shows a near symmetric two peaked curve. Stall occurs at an angle of attack of 16 degrees for the higher Reynolds number of 3,000,000 and the C_{lmax} has a value of 1.97. At this same Reynolds number the lesser peak at an angle of attack of 155 degrees has an identical value of lift coefficient, making the S815 lift curve at high Reynolds numbers truly symmetrical about ninety degrees.

When looking at the lower Reynolds number lift curve this symmetry is lost because of a reduction in lift coefficient at stall. At a Reynolds number of 100,000 roughness effects are also present with a 0.1 drop in lift coefficient from a C_{lmax} of 1.73 at stall for the smooth and rough surface scenarios. The scenario where transition is fixed on upper and lower surfaces has a higher C_{lmax} of 1.81 and does not exhibit this sudden drop in lift coefficient. Like the S814 section the trend of the lift curve recovers and rejoins the trend of the other curves at around forty degrees angle of attack, past which no Reynolds number or roughness effects are observed.

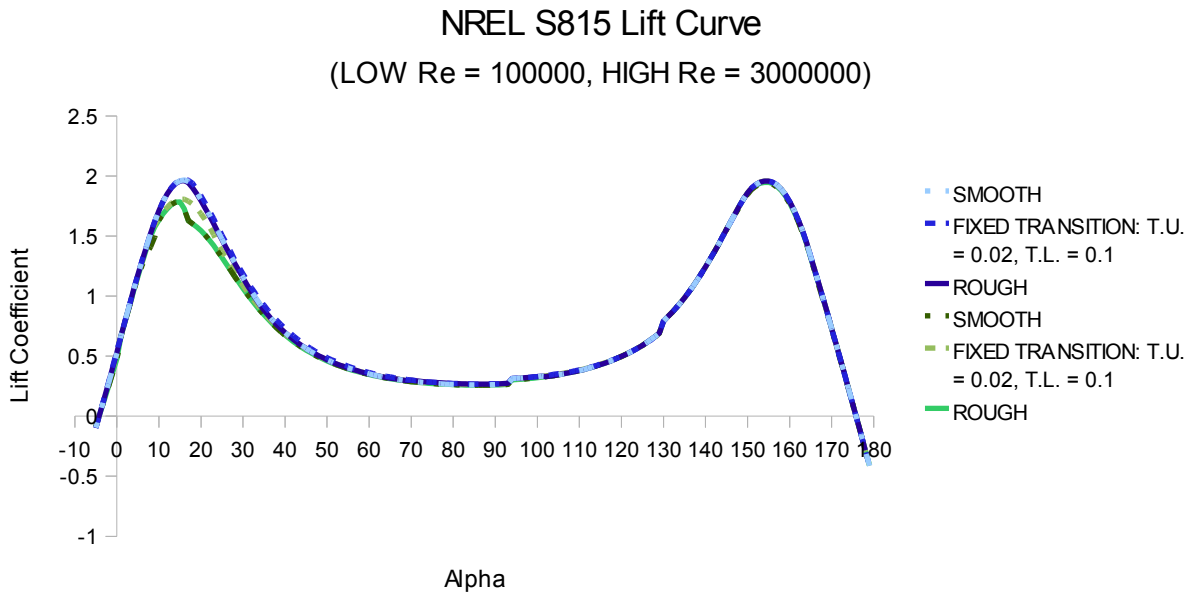

Figure 16: *S815 Lift Curve Plotted over alpha range -5<alpha<179 at low and high Reynolds numbers.*

The drag polar for the S815 is almost identical to that of the S814 with the exception of a higher C_{lmax} value. However, minor differences can be seen in the range of lift coefficient that the drag range remains below 1. The S815 drag coefficient only remains below 1 for lift coefficients of 0.8 and above.

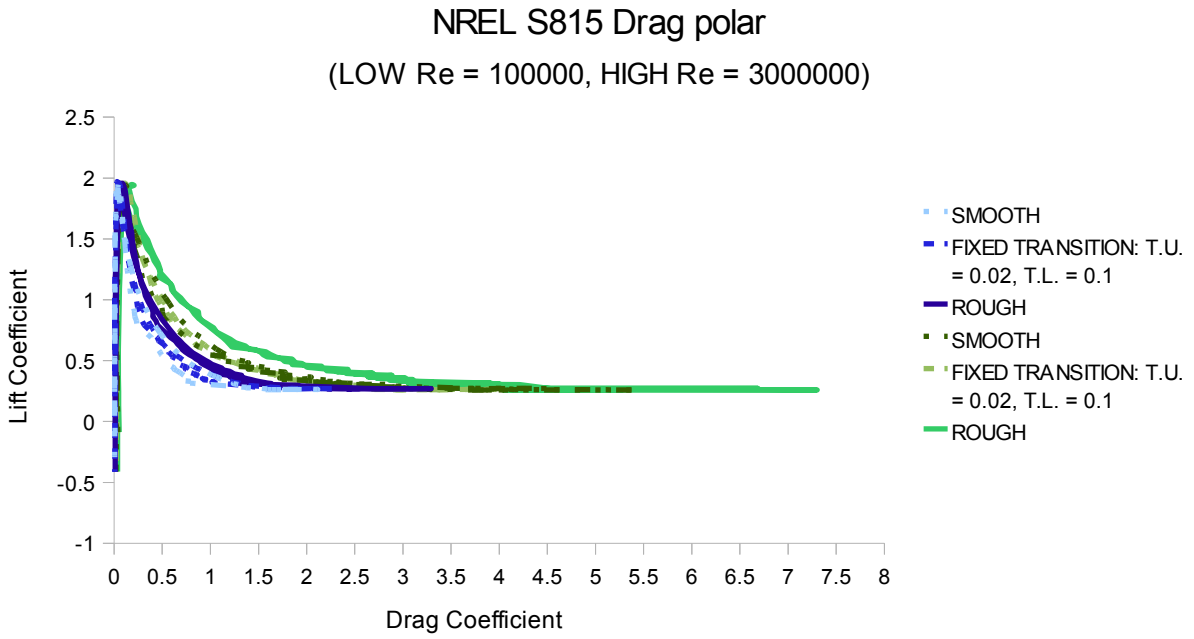

Figure 17: *S815 drag polar plotted over alpha range -5<alpha<179 at low and high Reynolds numbers*

5.3.4 An Introduction to NACA Section Families used in Turbine Design

The National Advisory committee for Aeronuatics (NACA) was the predecessor of the American space agency, NASA, and was formed during the First World War in order to surpass the, then more advanced, level of European Aviation. In its forty three years of research, before the formation of NASA in 1958, it dominated the world of Aerofoil testing and research (Rummerman, J. (2001)). It is because of this advanced research and testing that early wind turbine manufacturers used NACA sections for the turbine blades. Because of the analogous nature of tidal turbines the use of NACA sections was also transferable to marine technologies. However, with advancements in manufacturing and material technologies it is now commonplace for wind and tidal power devices to possess blades specially manufactured. Even if this is the case, most aerodynamic devices today are based in one way or another on NACA blade sections from one of the five "families" of NACA aerofoils in existence. NACA sections utilised in the design of existing wind and tidal turbines primarily belong to the four-digit, five-digit and 6-series families. NACA aerofoils are numbered by referring to designated section geometry and lift and drag characteristics.

For the purposes of this thesis only the 6-series family will be analysed because of their preferable post-stall lift characteristics and low sensitivity to roughness in comparison to the four and five-digit families (Abbott, I.H. & Doenhoff A.E.V. (1959)). The numbering system adopted by this family of aerofoils is commonly given in the form of a six digit number, as the name suggests. The first of these digits is always a 6 and simply designates that the section belongs to the 6-series family. The second digit denotes the chord-wise location of minimum pressure in tenths of the chord aft of the leading edge, which corresponds to the location of maximum thickness. Following these two numbers is often a comma followed by a single digit or this number can be displayed as a subscript. This single digit represents the range of lift coefficient in tenths above and below the design lift coefficient at which favourable pressure gradients on upper and lower surfaces are sustained. However, this may be replaced by three digits in parentheses that give the low-drag range and original thickness of a section that obtained its thickness distribution through linearly increasing or decreasing an existing sections ordinates. These two alternative numerical representations of lift and drag range characteristics are however not an available option in JavaFoil and to aid simplicity have been neglected from this analysis of NACA sections. These characteristics were also not stated for the NREL sections thus neglecting them also allows more accurate comparison between lift and drag characteristics. JavaFoil does however allow for values

to be input for 'a' and 'A', which respectively represent the mean line designation and thickness distribution modification. The mean line designation indicates the fraction of chord from the leading edge over which pressure distribution is uniform at the ideal angle of attack. The A denotes a modification to section thickness distribution in which surfaces are substantially straight from around 80% chord to the trailing edge. These two characteristics are also ignored in this analysis and therefore set to be unknown in JavaFoil i.e . a=1, A=0. The remaining three digits represent design lift coefficient in tenths and section thickness in percent chord (Hepperle, M (2006)).

For the purpose of this investigation into hydrodynamic performance of NREL and NACA aerofoils two NACA 63-xxx aerofoils were chosen to give a realistic comparison to the S814 and S815 sections. These NACA sections were purely hypothetical geometries based on the geometries of the two NREL sections and therefore designed to be geometrically identical in certain ways to their NREL competitors.

JavaFoil has thickness, thickness location, design lift coefficient, mean line designation and A-modification inputs available to the user. It was therefore chosen to make the thickness and design lift coefficient inputs of the NACA sections 24% and 26% and 1.3 and 1.1 respectively. The position of maximum thickness was also chosen to be at 0.3 x/c. This was chosen because of the NREL section designs having exceedingly far forward positions of maximum thickness and the consequent performance enhancement found through promotion of leading edge transition achieved through this design consideration. The NACA 6-series designations for these two section shapes are therefore 63-1324 and 63-1126. Though there are some identical design features of the NREL and NACA sections it is evident from the figures displaying the section shapes shown in the subsequent sections that the NACA and NREL sections differ distinctly in geometry. This will therefore lead to different hydrodynamic performance characteristics such as post-stall behaviour and lift and drag coefficients.

5.3.5 Hydrodynamic Performance of NACA 63-1324 Section

The 63-1324 section has been artificially designed using JavaFoil and has a maximum relative thickness of 24% chord at a relative position of 30% chord. It's design lift coefficient is 1.3, which dictates the degree of camber in it's design. The shape of the 63-1324 is shown in Figure 18.

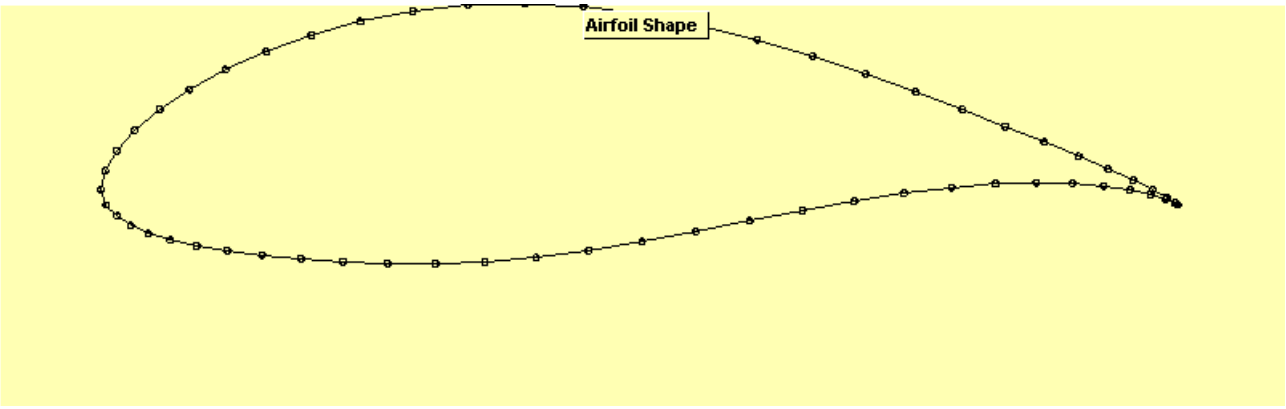

Figure 18: *63-1324 section shape created in JavaFoil*

The lift curves for low and high Reynolds number flow for the 63-1324 are displayed in Figure 19. The trend of the NACA section lift curve is somewhat different from that of the NREL sections with a greater disparity between the two peaks. The C_{lmax} of the section is affected by Reynolds number but does not appear to be influenced by surface roughness effects. Over the Reynolds number range 100,000 – 3,000,000 the C_{lmax} increases from 2.64 to 2.815. The second peak is substantially less at only 1.06 and like the NREL sections does not increase with Reynolds number. However a slight translation of the graph to the left as Reynolds number increases can be observed.

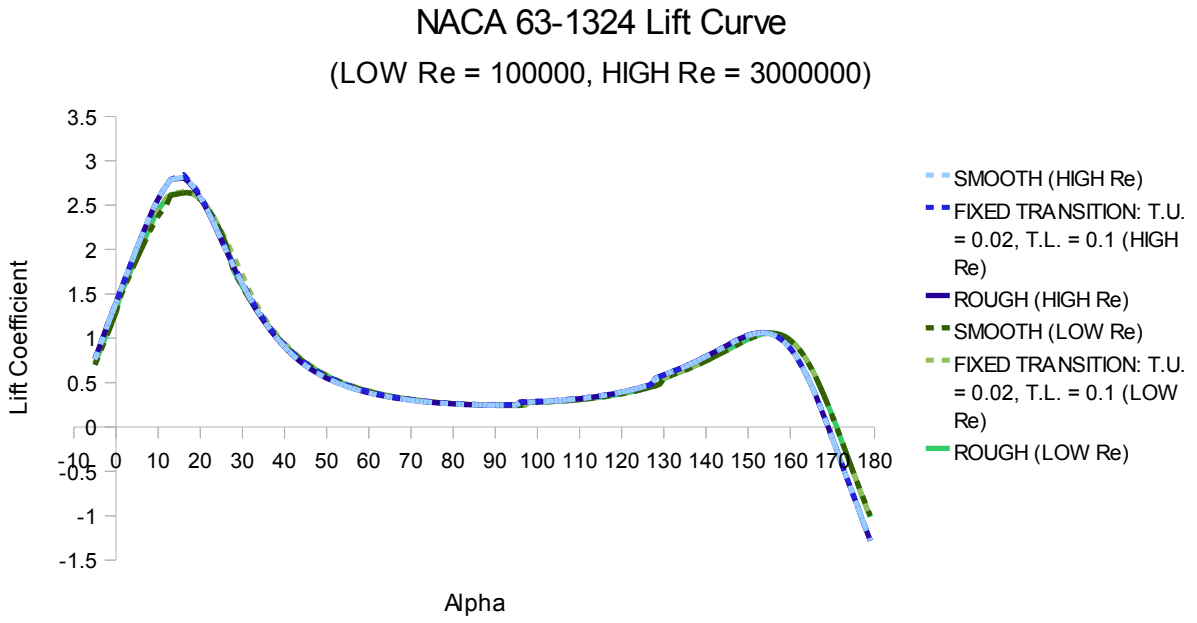

Figure 19: *63-1324 lift curve plotted over alpha range -5<alpha<179 at low and high Reynolds numbers*

The drag polar for the 63-1324 shown in Figure 20 exhibits lower maximum drag coefficient values than the NREL sections with it peaking at approximately 5 for the low Reynolds number flow and around half that for the high Reynolds number flow of the rough surface finish scenario.

Roughness effects are evidently greater at lower Reynolds numbers with a 1.5 reduction in drag coefficient at a Reynolds number of 100,000, whereas at a Reynolds number of 3,000,000 a reduction of less than 1 is observed between rough and smooth scenarios. The scenario with transition location fixed near the leading edge on upper and lower surfaces displays little difference in drag characteristics than that of the smooth scenario and at high Reynolds numbers these two scenarios are equal for most of the alpha range.

The minimum drag coefficient for the 63-1324 section is influenced by both Reynolds number and roughness and ranges from 0.005 to 0.021 for the smooth scenario over the Reynolds number range. For the rough scenario the minimum drag coefficient range increases to 0.011 to 0.037. the drag coefficient does not exceed 1 for lift coefficient values above 0.5 at high Reynolds numbers but this can only be said to be true for lift coefficient values above one in low Reynolds number flow. In fact the drag coefficient remains above 1 within the alpha range 42 – 128 degrees for low Reynolds number flow making this section impractical for low Reynolds number flow.

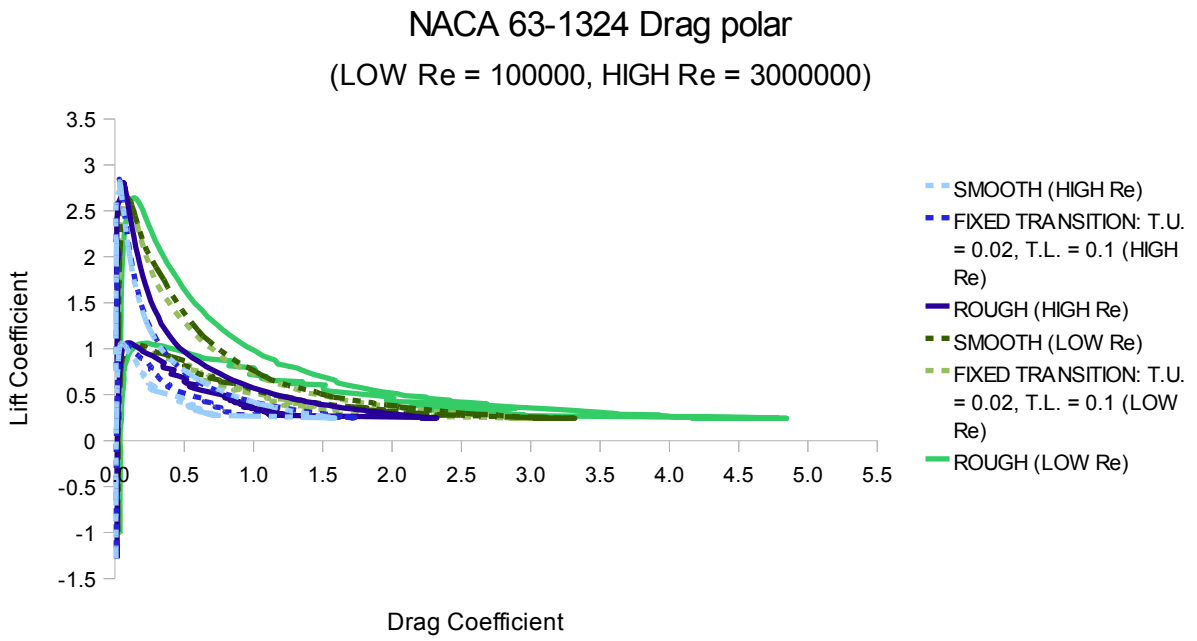

Figure 20: *63-1324 drag polar plotted over alpha range -5<alpha<179 at low and high Reynolds numbers*

5.3.6 Hydrodynamic Performance of NACA 63-1126 Section

As its NACA designation would suggest the 63-1126 is 26% thick at a relative position of 30% chord and has a design lift coefficient of 1.1. The result of these design constraints on section shape may be seen in Figure 21.

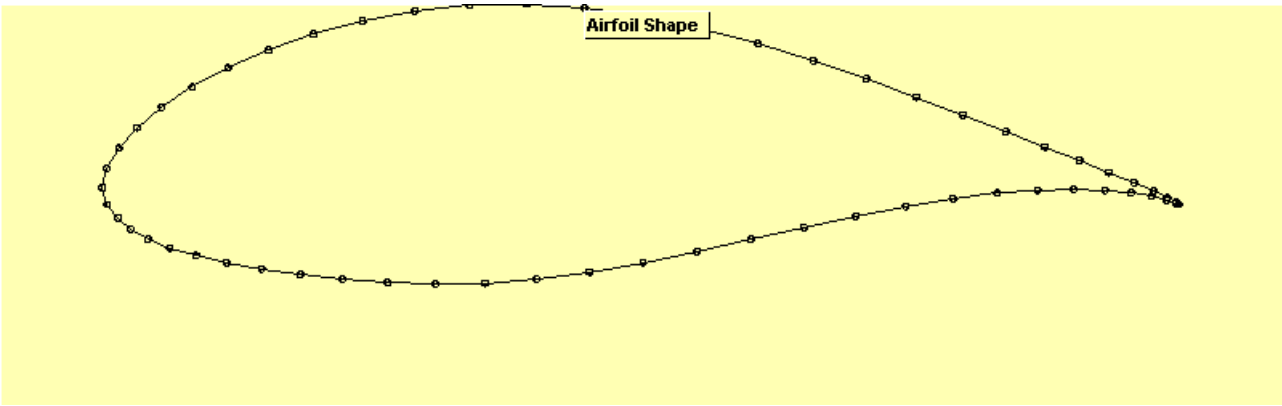

Figure 21: *63-1126 section shape created in JavaFoil*

The 63-1126 has a greater C_{lmax} than that of the 63-1324 as can be seen in Figure 22, which is insensitive to roughness effects but increases with Reynolds number. The C_{lmax} range for the 63-1126 starts at 2.58 at a Reynolds number of 100,000 and peaks at 2.75 in Reynolds number flow of 3,000,000. the effect of raising the lift coefficient is apparent up until an alpha value of around 50 degrees, beyond which Reynolds number does not have any effect on lift coefficient.

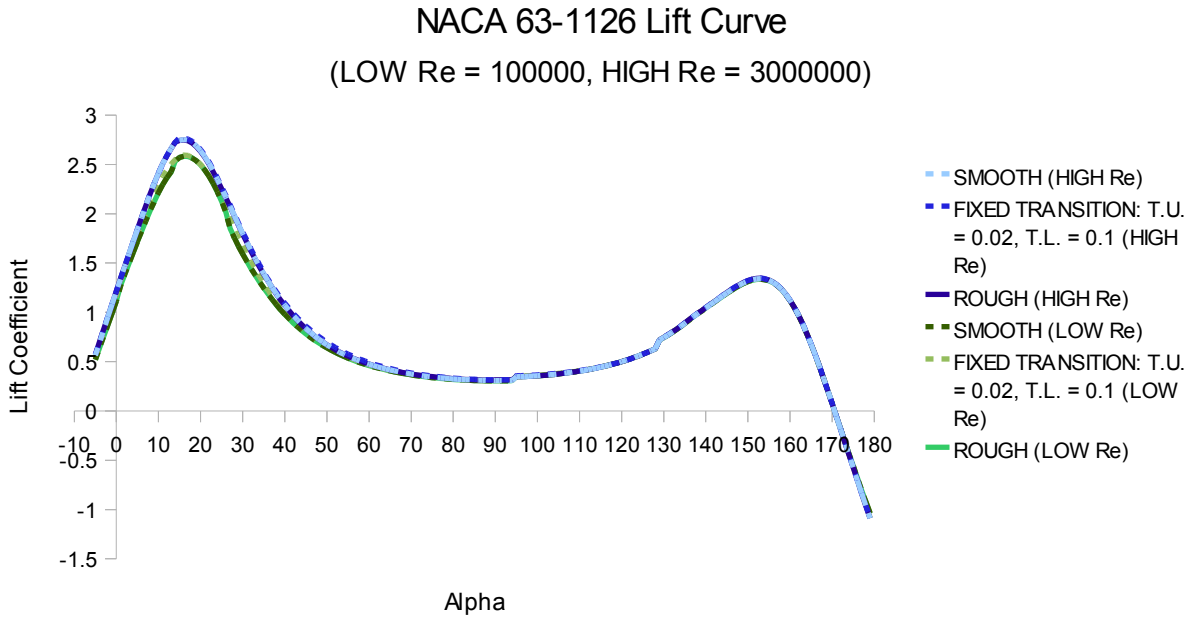

Figure 22: *63-1126 lift curve plotted over alpha range -5<alpha<179 at low and high Reynolds numbers*

The drag polar for the 63-1126 shown in Figure 23 shows a drag coefficient that is less sensitive to Reynolds number and roughness than that of the 63-1324. It can also be seen that this section has the lowest maximum drag coefficient of the four blade sections analysed in this chapter.

Roughness effects on drag coefficient appear to be less at low Reynolds number although when observing the difference in peak drag coefficient the difference between rough and smooth scenarios is almost identical for both low and high Reynolds number flow. This difference is approximately 0.5.

Reynolds number effects are more prominent and cause an increase from 0.005 to 0.021 for the

smooth scenario minimum drag coefficient and from 0.011 to 0.021 for the rough scenario. From Figure 23 it can also be noted that the lift coefficient range for which the drag coefficient remains below 1 is greater than that of the 63-1324 with all values below about 0.8 corresponding to a drag coefficient value of less than 1.

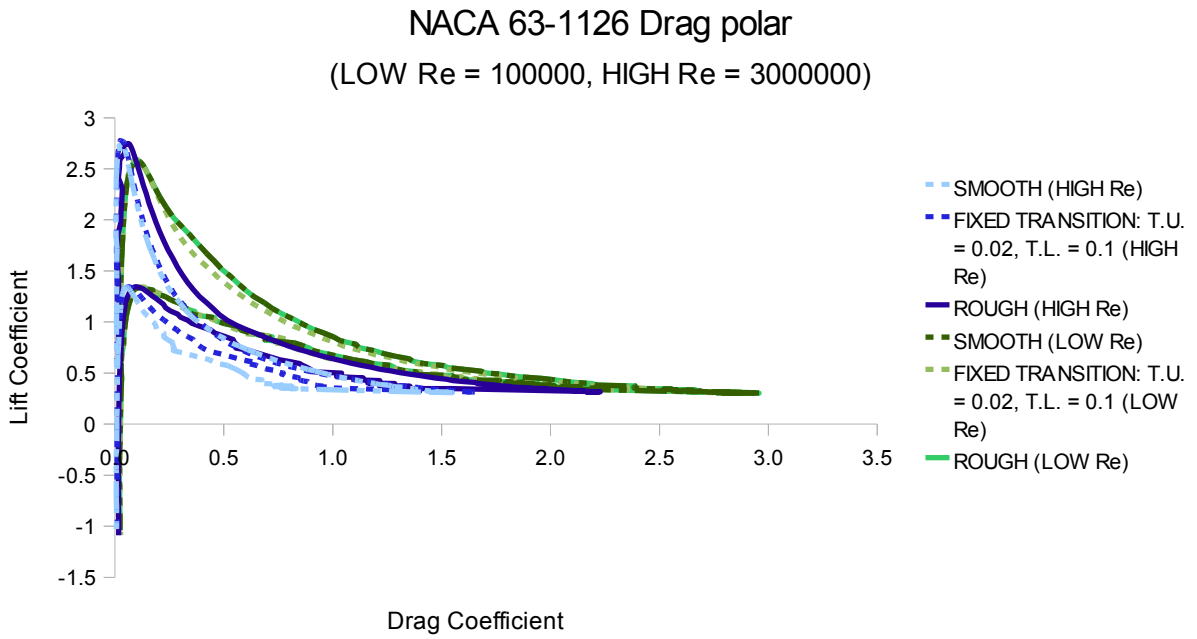

Figure 23: *63-1126 drag polar plotted over alpha range -5<alpha<179 at low and high Reynolds numbers*

5.3.7 Concluding Remarks on Blade Section Selection for a Tidal Stream Turbine

Having analysed four candidates for blade section for a tidal turbine a section from the NREL sections and from the NACA sections were selected to be used in the computational code described in chapter 6.

Of the two NREL sections analysed it was decided that the S814 would be used because of the greater lift coefficient range that the drag coefficient remained at a satisfactorily low level. A compromise in lower C_{lmax} was made by choosing the S814 over the S815 but low drag over a large lift coefficient range is a more important hydrodynamic characteristic when considering a turbine blade.

From the NACA sections analysed, the 63-1126 clearly performed better at low Reynolds numbers and maintained a lower drag coefficient for a greater range of lift coefficient. It also had a higher C_{lmax} and a higher lift coefficient for all values of alpha, therefore making it the obvious choice of the two NACA sections.

6 MODELLING OF THE CORMAT AND RESULTS

In this chapter a description of the BEMM implemented in MATLAB is presented as well as the corresponding graphical results obtained and a discussion of said results. These results are presented for both the NREL S814 and NACA 63-1126 aerofoils chosen in Chapter 5. The graphical results come in the form of performance curves often associated with rotor dynamics: thrust and power coefficients plotted as functions of tip speed ratio for different blade pitch angles. These two non-dimensional indicators of rotor performance allow a comparison of the CoRMaT device to existing rotor devices to be made and therefore the merits and drawbacks in terms of performance to be recognised. In the context of this thesis an indication as to which aerofoil would perform more to the CoRMaTs specification will be sought in terms of the aforementioned performance curves. It should also be mentioned at this point that the MATLAB models presented in this chapter deal with a single rotor device only but the theory behind the implementation of the BEMM on a contra-rotating device is presented in section 6.4.

6.1 Model Inputs and Parameters for a Single Rotor Device

In order to achieve a working model in MATLAB the inputs used in the model must first be defined. This is the first step in any computer program and consists of either constant values pre-defined in the program file or user defined inputs that are input during the running of the program. In the specific case of MATLAB user defined inputs are entered in the command window or through the use of a dialog box. These inputs may then be used at any point after they have been defined to calculate other parameters needed by the program. In the context of the blade element code presented here a mixture of pre-defined and user-defined inputs are used to calculate the model parameters and outputs. The outputs produced by the BEMM model were:

- Thrust coefficient performance curve
- Power coefficient performance curve

The following two subsections discuss the inputs and parameters categorised into user-defined and blade-section-specific categories.

6.1.1 User-defined Inputs and Parameters

For the model used in MATLAB some of the BEMM input values have to be defined by the user. These values are not section specific and are constant scalar values. They can therefore be entered by the user to model location-specific flow conditions. This was achieved by using MATLAB's *"input dlg"* function, which prompts the user to key in values through a dialog box that pops up when the program is run through the MATLAB editor window. Additional conditional statements then ensured that these inputs were within a certain tolerance and not empty arrays so as to give realistic results. This was achieved through creating a matrix of default values, associated with the CoRMaT device, that fall within a certain tolerance range. Coupled with a series of "*if*" statements this section of the code compares the values entered by the user with the matrix of expected values and if they fell outside the set range then a question dialog box appears asking if the user wishes to correct the erroneous values or start again. If the first of these two options was selected then the dialog box will pop up again for the user to change the values entered as zero or outside the tolerance. If the latter option was selected then the code will run from the beginning again. The user-defined inputs and their respective tolerance ranges consist of:

- Number of blades (1 - 10)
- Turbine tip radius (1 - 10 m)
- Turbine root radius (0.1 - 2 m)
- Number of blade elements (10 - 100)
- Rotor hub pitch angle (-80 - 80 degrees)
- Fluid density (950 – 1050 kg/m^3)
- Freestream flow velocity (0.1 – 20 m/s)
- Start value of TSR range to plot over (0 - 20)
- End value of TSR range to plot over (1 - 50)

For the purpose of plotting thrust and power coefficients over a range of tip speed ratios the TSR variable was defined as a vector of one hundred equally spaced values using MATLABs "*linspace"* command. The one hundred values span from the two values defined as the start and end TSR parameters. A "*for"* loop was then initialised to calculate the two performance coefficients over

this tip speed ratio range. From these model inputs there are a number of parameters that can be calculated in order to ascertain the inflow factors required to calculate power and thrust.

The first of these parameters is the radial position at which each iteration is carried out to evaluate blade element characteristics. This was set to be a vector, again, by using the "*linspace*" syntax but instead of using the default one hundred equally spaced points between the two chosen end points a third variable was introduced so that the number of points were equal to the number of elements defined in the rotor inputs. This was done using the following line of code:

```
R1 = linspace(Rr1,Rt1,nr);
```

where *Rr1* and *Rt1* are rotor one's root and tip radii respectively and *nr* is the number of elements.

Once the vector of radial positions along the span of the blade had been defined the blade chord and pitch angle could be ascertained. For the purpose of this thesis these two sets of values were specific to the CoRMaT device's blades. If the user wishes, the input data in the m-file can be replaced by other data taken at any number of radial stations desired. That is provided that the data is sorted into the same column order as observed in the m-file: Radial position [metres], chord [metres], blade pitch angle [degrees]. MATLAB's built in interpolation function, "*interp1,*" was then used to interpolate the input chord and pitch distribution data to give values for these variables at each of the fifty radial stations. The default method of interpolation for this function is linear so in order to increase the accuracy of the interpolation MATLAB was told to use piecewise cubic interpolation by the use of the string command "*cubic*." In addition to this the string command "*extrap*" was also used to extrapolate outside the data range for any calculated values that fell outwith the input data range. In relation to the calculation of the pitch angle an initial rotor hub pitch value was defined in the inputs to account for any degree of collective pitch that may be actuated. The lines of code that carry out this interpolation are as follows:

```
Theta = deg2rad(th0 + interp1(data(:,1),data(:,2),R1,'cubic','extrap'));
C = interp1(data(:,1),data(:,3),R1,'cubic','extrap');
```

These two values gave the following blade chord and pitch distributions:

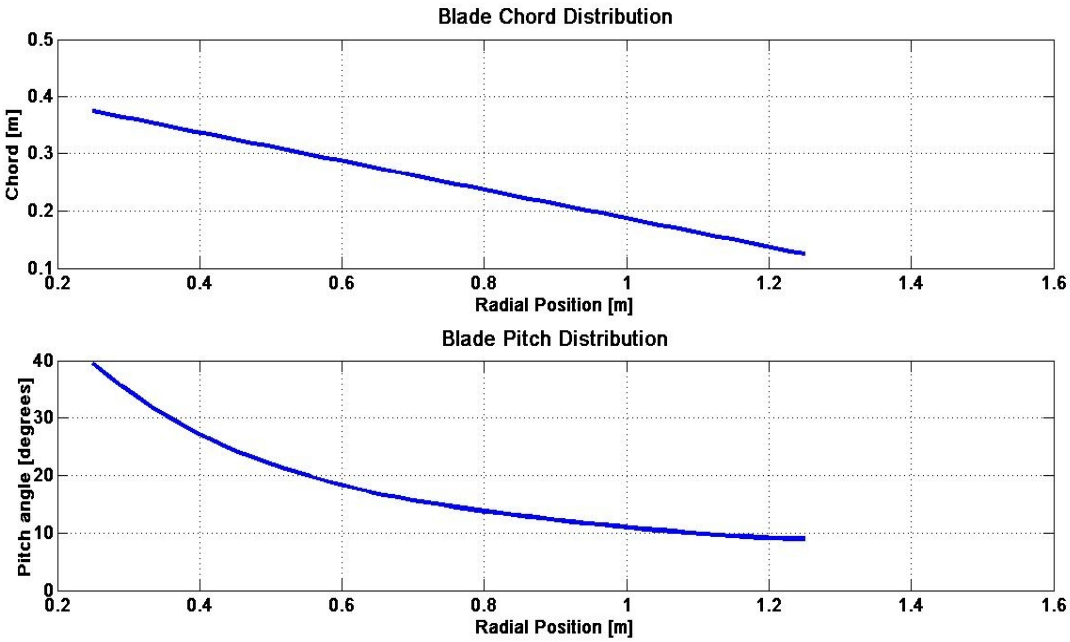

Figure 24: *CoRMaT Blade and Pitch distributions*

From the radial position vector the local solidity could be calculated using equation 3.25. Furthermore the turbine's rotational speed can be calculated using the following equation:

$$\Omega = \frac{U_t \times U_\infty}{R} \tag{6.1}$$

After these input parameters had been defined the next stage was to initialise a while loop used to iterate towards a solution for the inflow factors. Within this while loop there exist a number of parameters that are independent of blade section selection and are calculated from a combination of inputs and outputs.

The inflow angle is the first parameter to be evaluated inside the loop and is done so using equation 3.14. However it was not as simple as just taking the inverse tangent of the right hand side of the equation. Quadrant information was required therefore MATLAB's trigonometric function "*atan2*" was required to give accurate values. Knowledge of the inflow factors was also required to calculate this parameter therefore they had to be initialised before the loop. The initial values could have been any arbitrary value but for ease of implementation it was chosen for both a and a' to be

set to a vector of zeroes equal in size to *R1*. The first value for inflow angle was therefore evaluated for *a=a'=0.*

From the inflow factors and some of the user inputs the resultant velocity could be evaluated using equation 3.12 and similarly the angle of incidence could be found using equation 3.15.

As explained in sections 3.3.1 and 3.3.2 Prandtl and Glauert's correction factors can be incorporated into the BEMM to account respectively for a finite amount of blades and momentum method breakdown above a certain axial inflow factor. Incorporation of these in the MATLAB code is accomplished using equations 3.26-3.29, 3.34 and 3.35. A simple "*if*"statement was utilised to tell MATLAB that if *a* was less than 0.4 to use Prandtl's correction factor and if *a* was greater than or equal to 0.4 then to use Glauert's correction factor. This is depicted mathematically in sections 3.3.1 and 3.3.2.

6.1.2 Blade Section Specific Inputs and parameters

The rest of the inputs and parameters within the blade element code are specific to the blade section used. The majority of these quantities are based upon the aerodynamics of the blade section and therefore need to be obtained through the use of JavaFoil or from experimental data.

The first blade section specific quantities that appear in the code are lift and drag coefficients and the equations used to project them into normal and tangential components (equation 3.20). the lift and drag data for both the NREL S814 and NACA 63-1126 blade sections are included in the code and dependant on which of the two the user wishes to use the lift and drag coefficients at differing angles of incidence can be evaluated. This is again done using the "*interp1*" function and both "*cubic*" and "*extrap*" string commands. The extrapolation command is especially useful in this context if the lift and drag data in possession only covers a small angle of incidence range.

From these quantities it was possible to calculate the tangential and normal forces experienced by the rotor simply by multiplying by the normalising factor of C_N and C_T shown in equation 3.20.

```
FT = 0.5*rho*Ures.*Ures.*C.*Ct1;
```

```
FN = 0.5*rho*Ures.*Ures.*C.*Cn1;
```

6.1.3 Method of Iteration Adopted

In order to calculate the inflow factors at each radial station a "*while*" loop was used, which contained a logic statement:

```
while isdone == false
```

Starting the loop like this meant that an additional statement at the end of the loop could be used that ensured the iteration ran until it converged, at which point the logic statement became true. For this purpose an "*if*" statement was utilised in which one of two conditions had to be met. The first of these conditions was that if the difference between inflow factors of consecutive iterations was below a certain tolerance the loop had converged. The second was that if the iteration counter exceeded one thousand the logic statement became true. This statement looked as follows:

```
if   (max(max_abs_diff_a1,max_abs_diff_a_dash1) < 0.00001) || count >=
1000
    isdone = true;
end
```

where: `max_abs_diff_a1 = max(abs(a1 - a_new1));`
& `max_abs_diff_a_dash1 = max(abs(a_dash1 - a_dash_new1));`

This "*while*" loop was then nested within the "*for*" loop so as to calculate the inflow factors over the tip speed ratio range.

6.1.4 Model Outputs

In the introduction to this section the graphical outputs produced by said models were mentioned. Although this was done using four separate models the actual output data is identical for the non-dimensional performance curves and for the dimensional performance curves. The only coding that changes from model to model is the curve obtained after the code has finished running. This section therefore discusses, in general, the lines of code that deal with calculating these outputs and

the theory used.

In order to calculate the thrust and power for the rotor equations 3.21 were integrated numerically over the length of the blade. This was done using the trapezoidal rule, which conveniently MATLAB has a built-in function for. The "*trapz*" function uses the numerical integration scheme known as the trapezoidal rule to evaluate a given integral. In the case of rotor thrust and power the integral of normal and tangential forces along the radius of the rotor are required. The three following lines of code were written to carry out this integration and the result was multiplied by the number of blades to obtain the rotors overall thrust and power.

```
M = B1*trapz(R1,FT.*R1);

T = B1*trapz(R1,FN);

P = M*Omega1;
```

Where *M* is the torque of the rotor.

From these values the power and thrust coefficients could be easily calculated by using the following formulae to non-dimensionalise thrust and power:

$$C_T = \frac{T}{\frac{1}{2}\rho U_\infty^2 \pi R^2} \quad C_P = \frac{P}{\frac{1}{2}\rho U_\infty^3 \pi R^2} \tag{6.2}$$

These were evaluated within the for loop and therefore could be evaluated at each tip speed ratio to produce the required performance curve.

Finally the "*disp*" and "*plot*" commands were then again used to display the outputs at each tip speed ratio value and plot the two performance curves.

6.2 BEMM Model User's Guide

This section of the thesis takes the user through a step-by-step manual of the MATLAB codes and explains the method by which outputs can be obtained for an arbitrary tidal stream device.

As mentioned in section 6.1 the inputs can be split into two categories:

1. User-defined inputs
2. Blade-section-specific inputs

The first of these two categories consists of seven scalar values and one vector value defining the TSR range to be plotted over. In order to allow these to be easily defined by the user the MATLAB function "*inputdlg*" was utilised. The user must first run the code from the editor window by clicking on the green triangular icon highlighted by the red rectangle in the screen shot below:

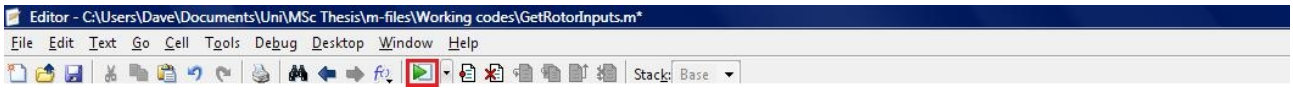

The user must then input a scalar value into each field of the dialog box. Once all inputs are defined the code runs and the performance plots are generated in the MATLAB figure window.

The user will then be asked if they want to run the code again with different inputs and the options *"Run again"* and *"Quit"* are available. If "*Run again*" is selected the code will run again and the new plot will be displayed in the figure window. If "*Quit*" is selected then the dialog box is closed and control of the MATLAB windows is returned to the user.

With respect to the second input category blade-section-specific quantities must be changed in the MATLAB editor window from which the code is run. This is a slightly more difficult procedure and must be done carefully to avoid erroneous results.

The first of these inputs is a matrix of dimensions m x 3 named "`blade_data`", where m is an undefined number of rows. The three columns in this matrix define the blade chord and pitch distributions over a number of blade radial stations. The number of blade radial stations used is up to the user as this data is later interpolated to produce vectors for chord and pitch values at each element in the BEMM. The order of the columns and rows is important and must follow the following template:

column 1: position of blade radial station in terms of blade radius in metres;

column 2: blade chord in metres at respective radial station;

column 3: blade pitch angle in degrees at respective radial station.

The order of the rows should follow consecutive blade elements from blade root to blade tip. To replace the existing data in this matrix it is as simple as copying and pasting the ordered data from a spreadsheet or notepad file into the square brackets and deleting the current data.

The only other blade-section specific data in the code is lift and drag coefficient data. This is input in the form of an m x 2 matrix consisting of coefficient data over an angle of incidence range. Again the number of rows is entirely up to the user. However, the greater the angle of incidence range the more likely it is that the outputs obtained are accurate predictions. This data is again interpolated and as described in section 6.1 the MATLAB "*extrap*" command is used to extrapolate outside the alpha range if necessary. Again the inputting of this data is as simple as deleting the existing data within the square brackets and replacing it with lift and drag coefficient data from a spreadsheet or notepad file.

6.3 Results and Discussion of Results for a Single Rotor BEMM Code

Two sets of results were obtained through the MATLAB BEMM code for each of the two selected blade sections. These come in the form of performance curves CT – TSR and CP - TSR and Power – Tidal Stream Velocity curves. From these curves a comparison between performance of each blade section could be made. It should be mentioned here that the lift and drag coefficients used in the following analysis were taken at a Reynolds number of 1.5 million. This is because it was the median value of the range of Reynolds numbers used in the chapter 5 analysis.

6.3.1. Comparison of CT – TSR Curves

The first of the performance curves produced using MATLAB was the CT – TSR curve for both the NREL S814 and NACA 63-1126 blade sections. The results over a tip speed ratio (TSR) range of 0-8 at three different blade pitch angles are presented in Figure 25.

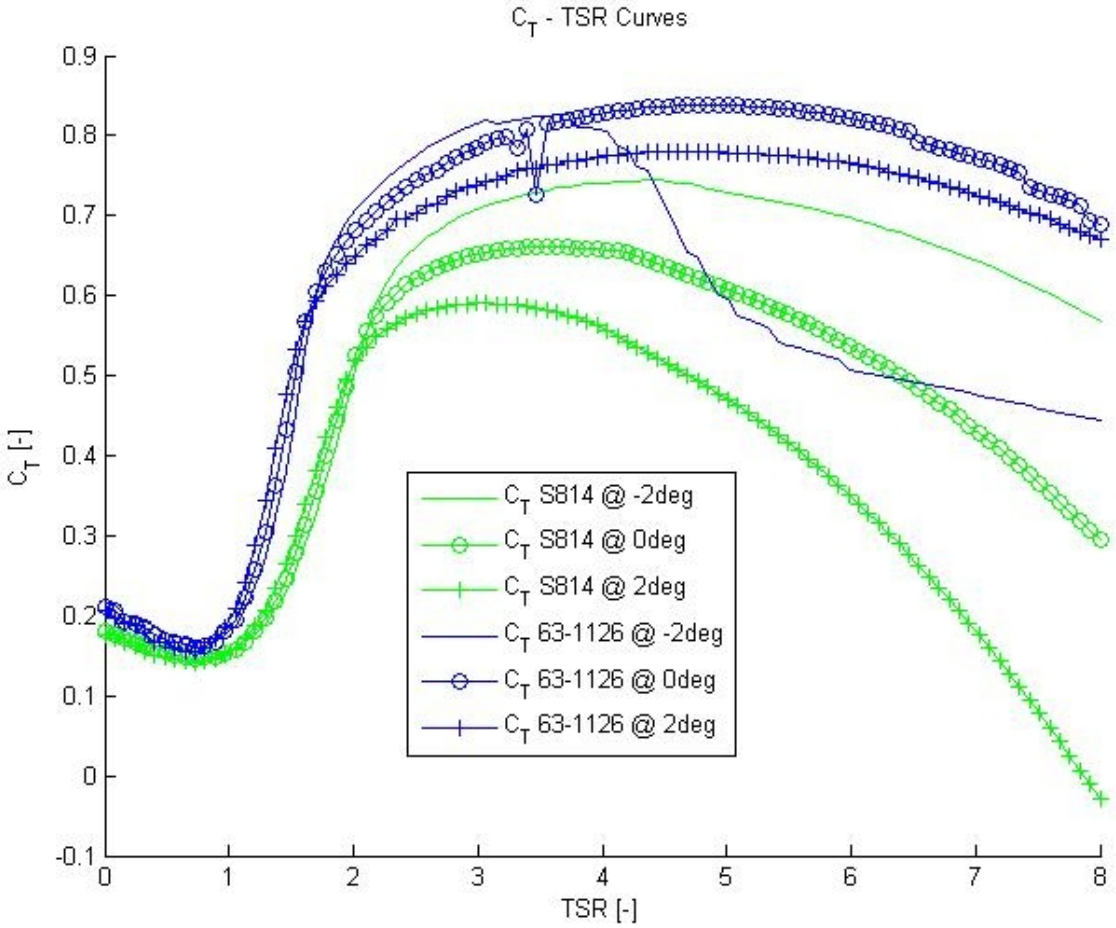

Figure 25: *Thrust Coefficient Performance Curves for NACA 63-1126 and NREL S814 Blade Sections for -2/0/2 Blade Pitch Angles*

It can clearly be seen that the NREL blade section has a lower thrust coefficient over the TSR range of 0-8 for all blade pitch angle settings. This is with the exception of the -2 degrees blade pitch setting at TSR values above four. Beyond this point the thrust coefficient of the NACA section falls below both that of the 0 and -2 degree blade pitch settings of the NACA section. This happens suddenly and not smoothly like all the other blade pitch settings, which implies that the blades may have stalled or that the results beyond this TSR for this blade section at the -2 degrees pitch setting are erroneous. The remainder of the results can be assumed to be accurate predictions of the turbines performance and indicate that overall the NREL blade section produces a lower thrust coefficient when in operation and therefore the thrust loading on the structure can be assumed to be less over the TSR range for a given blade pitch setting. This is a desirable performance characteristic because it indicates that the structure will display less fatigue from forces in the

normal direction. The optimum pitch setting for both blade sections appears to be +2 degrees because over a TSR of two the lowest thrust coefficient values are obtained for this pitch setting.

In terms of overall performance the NREL S814 exhibits an increasingly steeper gradient falling away from the peak thrust coefficient value as the blade pitch angle is increased. This is also a desirable design characteristic because this implies that the S814 would retain a considerably low thrust loading over a larger TSR range than the NACA section.

6.3.2. Comparison of CP – TSR Curves

The next performance characteristic analysed using the BEMM code was the power coefficient and Figure 25 presents the CP – TSR curves for both blade sections at the three blade pitch settings.

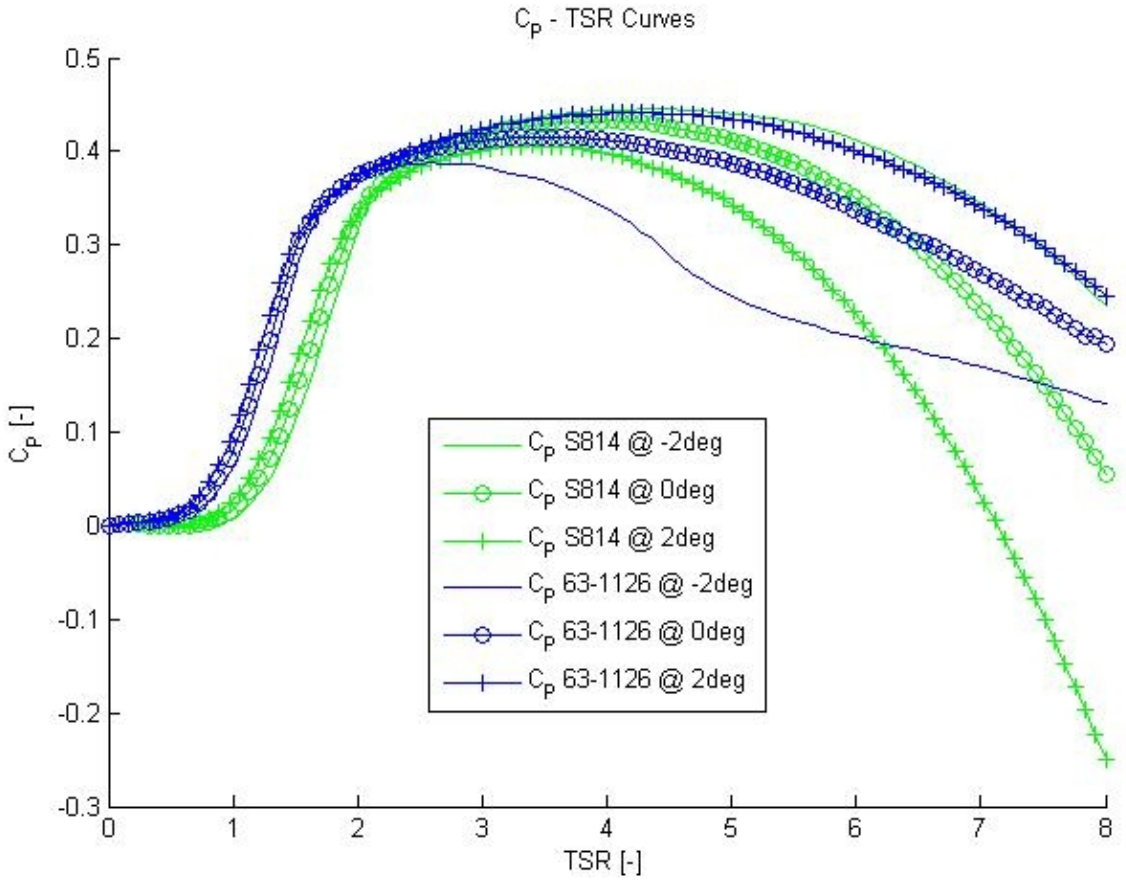

Figure 26: *Power Coefficient Performance Curves for NACA 63-1126 and NREL S814 Blade Sections for -2/0/2 Blade Pitch Angles*

It can be observed that the two blade sections exhibit inverse relationships with blade pitch and maximum power coefficient. As the blade pitch is increased the NACA section's maximum CP increases, whereas the NREL section's maximum CP decreases. This is most obvious for TSR values greater than three. The optimum blade pitch setting in terms of power coefficient for the NACA section is therefore +2 degrees and conversely for the NREL section it is -2 degrees. In fact, for TSRs greater than 3 these two curves show remarkably similar trends. However, the NREL blade section was observed to have a marginally greater maximum CP value of 0.4451, in comparison to the NACA section's value of 0.4412.

In terms of steepness in gradient after the maximum value the NACA section performs better because it retains a higher power coefficient value over a larger TSR range for all three blade pitch settings.

6.4 BEMM Applied to a Contra-rotating Device

In order to extend the model for a single rotor device to a contra-rotating device a few assumptions have to be made in terms of the inflow factors and torque balancing between the two rotors. This is because there are now too many unknown variables to solve for and not enough equations to do so.

The first of these assumptions is that the rotors are of a negligible distance apart therefore allowing them to be treated as one actuator disk. The second is that the swirl induced on the flow by the first rotor is negated by the second rotor. This has implications on the tangential inflow factor and it is therefore assumed that this value at the second rotor exit is zero.

In order to obtain a closed solution to the BEMM equations for a contra-rotating pair of rotors these assumptions must all be utilised. The results from the BEMM carried out on the first rotor are also required but with an additional assumption made with regards to axial thrust loading. The existence of two co-axial rotors now means that both rotors experiences a share of the overall forcing experienced by the fluid stream. This therefore has an effect on the BEMM equations presented in section 3.3.

6.4.1 Changes to the BEMM Equations for First Rotor

The only fundamental change to the BEMM equations for the first rotor occurs because of the sharing of axial thrust loading between the two rotors. This ratio of axial thrust between the two rotors obviously has implications on the structural loadings, especially on the blades, and upon performance. The optimum ratio is, as yet, unknown and only through simulation and experimentation may it be found. The simulation results obtained for the first rotor in this thesis are the first steps to finding this optimum configuration.

For the purposes of this thesis it was assumed that the rotors shared the axial thrust loading equally therefore giving a 1:1 axial thrust loading ratio. Equation 3.26 then becomes:

$$dT_1 = 2\pi r \rho U_\infty^2 a(1-a) F dr \tag{6.3}$$

This therefore has an effect on the axial inflow factor equation (equation 3.29), which becomes:

$$a = \frac{1}{\frac{2F\sin^2\varphi}{\sigma C_N} + 1} \tag{6.4}$$

Where all of the subscript number ones indicate that these values denote rotor one variables. The rest of the equations remain unchanged for the first rotor.

6.4.2 BEMM Equations for the Second Rotor

For the second of the contra-rotating pair of rotors the majority of the BEMM equations required to solve for the inflow factors are identical to those used for the first rotor calculations. The assumptions that result in a few discrepancies between rotor equations are that the tangential inflow factor at the second rotors exit is zero and that the axial thrust loading is shared between the two rotors. The first of these has implications on the inflow angle given by equation 3.14.

$$\tan\varphi = \frac{(1-a)U_\infty}{\omega r} \tag{6.5}$$

This assumption also has implications on the torque transferred to the freestream and if the final tangential inflow factor is zero then this will be identical for both rotors i.e. $dM_1 = dM_2$, where the subscripts again denote upstream and downstream rotor parameters. The equivalent of equation 3.11 for the downstream rotor is then:

$$dM_2 = 4\pi r^3 \rho U_\infty \omega (1-a) a' dr \tag{6.6}$$

In general this does not hold for the axial thrust i.e. $dT_1 \neq dT_2$. In this case, however, the axial thrust loading is shared equally between the two rotors therefore the two equations are the same:

$$dT_2 = 2\pi r \rho U_\infty^2 a (1-a) dr \tag{6.7}$$

If an optimum axial thrust loading ratio were to be sought then the two value in the denominator of equation 6.4 could be made manually variable and a range of simulations run. Alternatively an iterative solution could be sought through computational methods given certain design criteria. The solution desired would be dependant on whether the aim was to reduce thrust loading or optimise power output. This could be achieved by rearranging equations 6.4 and 3.29 for axial and tangential inflow factors in terms of solidity and equating them. An equation in terms of a ratio of tangential and axial forces on the downstream rotor could then be obtained in the form:

$$\frac{F_{T2}}{F_{N2}} = \frac{2a'(1-a)}{a} \tag{6.8}$$

A range of blade pitch angles for the downstream rotor could then be input until a solution is found.

The outputs obtained from implementing such a computational model would be blade pitch and chord.

7 CONCLUSIONS & FUTURE RECCOMENDATIONS

The aims of this thesis were to investigate the performance of a tidal turbine with the aid of Mathwork's MATLAB and in particular highlight the advantages of a contra-rotating tidal turbine over the more conventional single rotor tidal turbine.

Two blade sections were selected to be analysed through a hydrodynamic performance investigation in Chapter 5: The NACA 63-1126 and NREL S814 sections. The data created using JavaFoil was then used in the MATLAB BEMM code to produce non-dimensional performance plots of power and thrust coefficient as a function of tip speed ratio.

These performance plots, found in chapter 6 of this thesis, suggest that the NREL section currently used on the CoRMaT turbine performs more efficiently than the NACA section. With lower thrust coefficient values over the TSR range and consistently higher power coefficient values for varying pitch angles the NREL S814 exhibits more desirable performance characteristics. The introduction of a second rotor would suggest even lower values of thrust loading from the theory presented. At the design TSR of 3 the front rotor of the CoRMaT, device using the NREL S814 blade section, can be expected to produce thrust coefficient values ranging from approximately 0.55 – 0.7. This range of values are for blade pitch angles of -2,0 and 2 degrees with the lowest thrust loading being exhibited at the +2 degrees blade pitch setting. With respect to power performance the NREL and NACA sections exhibit similar characteristics but the NREL section performs consistently over the range of pitch angles whereas the NACA section has a drop in power output at the -2 blade pitch setting. The NREL section also shows less drop in power coefficient as the pitch angle is altered making it the better performer in terms of both performance indicators.

It would be assumed that these values would only improve with the addition of a second rotor. It can then be concluded that the NREL S814 is the best choice for the CoRMaT turbine and that NACA sections of similar profiles to those of the NREL S814 and S815 do not perform as well in terms of power and thrust performance.

Future Recommendations:

- Future developing of the work done in this thesis could be done to expand the MATLAB code to predict the performance of a contra-rotating tidal turbine and plot the performance curves for both one and two rotors in operation. This would give an indication of the actual improvement in performance achieved by using a contra-rotating configuration over a single rotor configuration.

- Once a working MATLAB code for a contra-rotating tidal turbine was achieved the introduction of a user-defined parameter to alter the thrust balancing between the two rotors. This would allow for easy optimisation of a contra-rotating rotor and further analysis of the wake structure at this optimised configuration.

- Another adaptation that could be made to the MATLAB code is amending it so that it could produce dimensional plots such as thrust and power against tidal velocity.

- With the code used in this thesis verification of results was done using blade and aerodynamic data for an existing helicopter rotor but blade pitch and chord distributions of another tidal turbine have not been analysed. It would therefore be a useful test of the codes accuracy if the code were run with experimental data of a single rotor tidal turbine currently in operation. A comparison of the simulated results and empirical data could then be made to further validate the BEMM code.

- When calculating the forces and torque of the whole turbine the trapezoidal rule was used to sum up these values over the elements. This could potentially be replaced by a higher order numerical scheme, such as a Runge-Kutta integration, to produce more accurate results.

- With regards to input data, which is currently embedded within the MATLAB code, an alternative and tidier way of calling the data would be to use the *xlsread* function. This allows the user to call data into the MATLAB domain from a spreadsheet of data by row and column references.

- In this thesis blade profiles were analysed with the same profile for the entire length of the blade. A logical progression to this would be to use data from different blade sections for root and tip sections of the blade.

- Finally an investigation into the forces experienced at the blade root of a contra-rotating turbine would verify whether these forces and moments are reduced for a contra-rotating configuration. If this were proven to be true then this would present a distinct advantage over single rotor configurations as current problems found in operational tidal turbines occur due to blade fatigue.

BIBLIOGRAPHY AND REFERENCES

Abbott, I.H. & Doenhoff A.E.V. (1959). *"THEORY OF WING SECTIONS Including a Summary of Airfoil Data."* Dover publications. U.S.A.

Aviation Enterprises Limited *"Composite Tidal Turbine Blade Design & Development"* Accessed on August 12th 2009 from:
www.pdf-search-engine.com/**turbine-blade-design**-pdf.html

Bak, C. et al (1999) "*Airfoil Characteristics for Wind Turbines."* Technical University of Denmark.

Baker , A.C. (1991). *"Tidal Power."* Peter Penguins Ltd. UK.

Batten, W.M.J. Et al (2006) *"Hydrodynamics of marine current turbines"* Renewable Energy 31 (2006) 249–256. Science Direct. Sustainable Energy Research Group, University of Southampton, UK.

Batten, W.M.J. et al (2008) "*The prediction of the hydrodynamic performance of marine current turbines."* RenewableEnergy33(2008)1085–1096. Science Direct. Sustainable Energy Research Group, University of Southampton, UK.

Blue Energy Canada Inc. (2008). *"Tidal Power."* Canada.
http://www.bluenergy.com/TidalPower.htm

Breslin, J.P. & Andersen, P (1996), *"Hydrodynamics of Ship Propellers."* Cambridge Press

Buhl, M.L. Jnr (2005). "*A New Empirical Relationship between Thrust Coefficient and Induction Factor for the Turbulent Windmill State."* NREL/TP-500-36834. U.S.A.

Burton, T. et al (2001). *"Wind Energy Handbook."* Wiley. UK

California Energy Commission (2003). *"Counter Rotating Wind Turbine System."* Accessed on 30th August 2009 from:
http://www.energy.ca.gov/pier/portfolio/Content/Completed97to06/Completedprior05plusEISG05/Counter%20Rotating%20Wind%20Turbine.htm.

Clarke, J.A. (2004). *"Output Characteristics of Tidal Current Power Stations."* ESRU. UK.

Clarke, J.A. Et al (2007). *"Development of a Contra-Rotating Tidal Current Turbine and Analysis of Performance"* ESRU. UK.

Cowles, G. et al (2009). *"An Assessment of the Tidal Kinetic Energy Resource off the Massachusetts Coast and Potential Impacts of Extraction."* Accessed on 20 September 2009 from:
http://www.smast.umassd.edu/CMMS/Site/MIT_SeaGrant.html

DNV & Risø, (2002) *"Guidelines for Design of Wind Turbines"* Det Norske Veritas, Copenhagen and Wind Energy Department, Risø National Laboratory.

EMEC (2008). *"Tidal Devices."* Accessed on 11th August 2009 from: http://www.emec.org.uk/tidal_devices.asp

European Commission (2008). *"The EU's Target For Renewable Energy: 20% by 2020, Volume 1: Report."* The Stationary Office Limited. UK.

Folley, M. et al (2006) "*Comparison of LIMPET contra-rotating wells turbine with theoretical and model test predictions."* School of Civil Engineering, Queen's University. UK.

Grant, A.D. et al (2007). *"Design and Testing of a Contra-rotating Tidal Current Turbine."* IMechE Vol. 221 Part A.

Glauert, H. (1935). *"Airplane Propellers."* Aerodynamic Theory (W. F. Durand, ed.). Div. L, Chapter XI. Berlin:Springer Verlag.

Grabbe, M. (2008). "*Marine Current Energy Conversion"* Uppsala Universitet.

Gregorek, G.M. (1988). "*Comparison of Pressure Distributions on Model and Full-Scale NACA 64-621 Airfoils With Ailerons for Wind Turbine Application"* Ohio State University. U.S.A.

Hansen, M.O.L (2008). *"Aerodynamics of Wind Turbines,"* Earthscan, UK & USA.

Hepperle, M (2006). "*JavaFoil – Analysis of Airfoils."* Accessed on the 13th July from: http://www.mh-aerotools.de/airfoils/javafoil.htm

Fofonoff. in The Sea, "*Vol. 1: Physical Properties of Seawater"* Accessed on the 20th July 2009 from: www.whoi.edu/science/PO/people/tjoyce/.../course_notes_1b.pdf

Francis, M. & Hamilton, M. (2007). "*SRTT Floating Tidal Turbine Production Design Study with Independent Verification."* BERR. UK

HM Government (2009). "*The UK Renewable Energy Strategy."* Crown Copyright. UK.

Ingram, G. (2005). "*Wind Turbine Blade Analysis using the Blade Element Momentum Method.* Version 1.0." Durham University. U.K.

IT Power (2005). *"Development, Installation and Testing of a Large-Scale Tidal Current Turbine."* Crown Copyright. UK

Kulunk, E. (2009) "*COMPUTER-AIDED DESIGN AND PERFORMANCE ANALYSIS OF HAWT BLADES."* IATS, Karabük University. Turkey

Law, S.P. & Gregorek, G.M (1987)*"Wind Tunnel Evaluation of a Truncated NACA 64-621 Airfoil for Wind Turbine Applications"* DOE/NASA/0330-2 NASA CR-180803. Ohio State University. USA.

McCombes, T. et al (2006). *"Marine Current Resource and Technology Methodology."* Accessed on 10th June 2009 from:
http://www.esru.strath.ac.uk/EandE/Web_sites/05-06/marine_renewables/home

Marsh, G. (2004). *"Tidal Turbines Harness the Power of the Sea."* Reinforced Plastics.

NASA (2000). "*Interplanetary Low Tide.*" Accessed on 6th June 2009 from:
http://science.nasa.gov/headlines/y2000/ast04may_1m.htm.

Nicholls-Lee, R. (2007). *"Simulation Based Optimisation of Marine Current Turbine Blades."* University of Southampton. UK.

Reaction Engines Limited (2006). *"Contra-rotating Turbines."* Accessed on 12th Aug from:
http://www.reactionengines.co.uk/contraturbines.html

REUK (2006). *"BETZ LIMIT: Understand the Betz limit and how it affects wind turbines."* Accessed on 4th Aug 2009 from:
http://www.reuk.co.uk/wind.htm

Reinforced Plastics (2008). "*Tidal turbine features composite rotors.*"

Rumerman, J. (2001). *"The National Advisory Committee for Aeronautics (NACA)."* Accessed on 28th July 2009 from:
http://www.centennialofflight.gov/essay/Evolution_of_Technology/NACA/Tech1.htm

Somers, D.M. (2004). *"The S814 and S815 Airfoils."* NREL. U.S.A.

Spera, D.A. (1994). *"Wind Turbine Technology."* ASME Press. U.S.A.

Sustainable Development Commission (2007). *"Turning the Tide: Tidal Power in the UK."* UK.

Tangler, J.L. & Somers, D.M. (1995). "*NREL Airfoil Families for HAWTs.*"

Timmer, W.A. (2009). "*An overview of NACA 6-digit airfoil series characteristics with reference to airfoils for large wind turbine blades.*" AIAA 2009-268. Delft University Wind Energy Research Institute, DUWIND, The Netherlands.

Thake, J., IT Power (2005). *"Development, Installation & Testing of a Large-scale Tidal Current Turbine."* Crown Copyright. UK

UNFCCC (2008). *"Kyoto Protocol Reference Manual on Accounting of Emissions and Assigned Amount."*

Varvill, R. et al (2008). *"DESIGN AND TESTING OF THE CONTRA-ROTATING TURBINE FOR THE SCIMITAR PRECOOLED MACH 5 CRUISE ENGINE."* IAC-08-C4.5.3